Direct Arp2/3-vinculin binding is required for pseudopod extension, but only on compliant substrates and in 3D

Tadamoto Isogai, Kevin M Dean, Philippe Roudot, Evgenia V Azarova, Kushal Bhatt, Meghan K Driscoll, Shaina P Royer, Nikhil Mittal, Bo-Jui Chang, Sangyoon J Han, et al.

iScience

Article

Direct Arp2/3-vinculin binding is required for pseudopod extension, but only on compliant substrates and in 3D

Graphical abstract

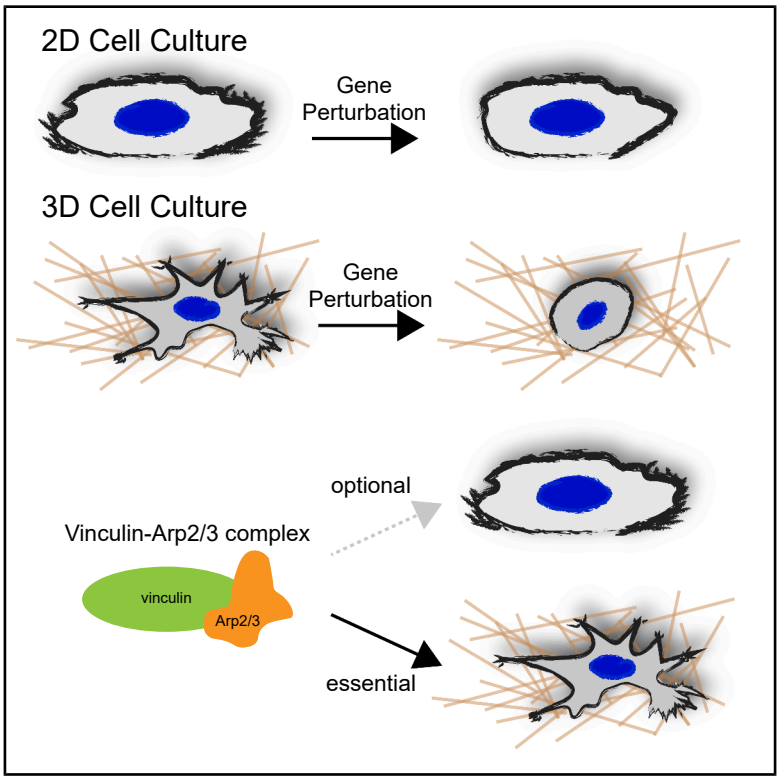

Authors

Tadamoto Isogai, Kevin M. Dean, Philippe Roudot, ..., Sangyoon J. Han, Reto Fiolka, Gaudenz Danuser

Correspondence

tadamoto.isogai@utsouthwestern.edu (T.I.), gaudenz.danuser@utsouthwestern.edu (G.D.)

In brief

Biological morphology; Molecular biology; Cell biology

Highlights

- Knockout of actin-binding genes yields differential phenotypes in 2D and 3D
- Arp2/3 promotes nascent adhesion formation especially on soft ECM substrates
- Arp2/3-vinculin interaction is dispensable for pseudopod extensions in 2D
- In contrast, Arp2/3-vinculin interaction is critical for pseudopod extension in 3D

Isogai et al., 2025, iScience *28*, 112623
June 20, 2025
https://doi.org/10.1016/j.isci.2025.112623

CellPress

iScience

CellPress
OPEN ACCESS

Article

Direct Arp2/3-vinculin binding is required for pseudopod extension, but only on compliant substrates and in 3D

Tadamoto Isogai,[1,2,3,5,*] Kevin M. Dean,[1,2,3] Philippe Roudot,[1] Evgenia V. Azarova,[1] Kushal Bhatt,[1] Meghan K. Driscoll,[1] Shaina P. Royer,[4] Nikhil Mittal,[4] Bo-Jui Chang,[2,3] Sangyoon J. Han,[4] Reto Fiolka,[1,2,3] and Gaudenz Danuser[1,2,3,*]

[1]Lyda Hill Department of Bioinformatics, University of Texas Southwestern Medical Center, Dallas, TX 75390, USA
[2]Department of Cell Biology, University of Texas Southwestern Medical Center, Dallas, TX 75390, USA
[3]Cecil H. and Ida Green Center for Systems Biology, University of Texas Southwestern Medical Center, Dallas, TX 75390, USA
[4]Department of Biomedical Engineering, Michigan Technological University, Houghton, MI 49931, USA
[5]Lead contact
*Correspondence: tadamoto.isogai@utsouthwestern.edu (T.I.), gaudenz.danuser@utsouthwestern.edu (G.D.)
https://doi.org/10.1016/j.isci.2025.112623

SUMMARY

A critical step in cell morphogenesis is the extension of actin-dense pseudopods, controlled by actin-binding proteins (ABPs). While this process is well-understood on glass coverslips, it is less so in compliant three-dimensional environments. Here, we knocked out a series of ABPs in osteosarcoma cells and evaluated their effect on pseudopod extension on glass surfaces (2D) and in collagen gels (3D). Cells lacking the longest Arp3 gene variant, or with attenuated Arp2/3 activity, had the strongest reduction in pseudopod formation between 2D and 3D. This was largely due to reduced activity of the hybrid Arp2/3-vinculin complex, which was dispensable on glass. Our data suggests that concurrent formation of actin branches *and* nascent adhesions, supported by Arp2/3-vinculin interactions, is essential to form mechanically stable links between fibrous extracellular matrix and actin in 3D. This highlights how experiments on stiff, planar substrates may conceal actin architectural features that are essential for morphogenesis in 3D.

INTRODUCTION

Cell shape control is impacted by extracellular matrix (ECM) mechanics, composition, and architecture.[1,2] In cooperation with integrin-based adhesion complexes,[2,3] actin and actin-binding proteins (ABPs) integrate these ECM cues to orchestrate force generation and morphological adaptation.[1,2,4–8] Some of our most detailed understanding of the mechanism of cell morphogenesis stems from experiments performed on glass slides or tissue culture plastic. On these planar surfaces (2D), cells are generally able to extend pseudopods without restriction, resulting in a flat morphology accompanied with abundant formation of filamentous actin (F-actin) stress fibers terminated by adhesion complexes (Figure 1A). When the same cells are embedded in a three-dimensional (3D) reconstituted matrix, such as collagen gels, they adopt a multipolar branched morphology with diminished stress fiber formation[11–14] (Figures 1B and 1C). These results highlight critical differences in F-actin cytoskeleton organization and pseudopod projection, when moving from 2D to 3D environments.[5,7,15–18]

While the field has accumulated profound understanding of how ABPs contribute to the formation of relatively flat pseudopods on stiff glass coverslips, much less is known how they contribute to the formation of multipolar pseudopodial projections found in 3D cell cultures.[4] To address this question, we knocked-out a set of actin regulators in U2OS osteosarcoma cells using CRISPR/Cas9 and quantitatively evaluated the effect of each on pseudopod extension in 2D and 3D environments. We find that pseudopod formation is more sensitive to loss of Arp2/3 activity in 3D environments than on flat and stiff 2D substrates. Among the Arp2/3-interacting focal adhesion proteins,[19–22] vinculin depletion phenocopied the context dependent pseudopod extension defect. This sensitivity partially hinges on the assembly of a hybrid Arp2/3-vinculin complex, which is fully dispensable during pseudopod formation on mechanically stiff 2D surfaces. This underlines the remarkable differences in the molecular requirements some of the core cell functions pose between 2D and 3D.

RESULTS

Knockout of actin-binding genes yields differential phenotypes in 2D and 3D

To gain insight into the roles that ABPs play in supporting cell morphogenesis in 2D and 3D environments, we performed a targeted CRISPR/Cas9-mediated knock-out (KO) screen of formins (mDia1/*DIAPH1*, mDia2/*DIAPH3*, FHOD1/*FHOD1*, FMNL1/*FMNL1*, FMNL3/*FMNL3*, INF2/*INF2*),[23] the Arp2/3 complex subunit Arp3 (Arp3/*ACTR3*),[18] Arp2/3 complex-activating nucleation promoting factors (NPFs: Wave2/*WASF2,* N-WASP/*WASL,* cortactin/*CTTN*),[17] F-actin side-binding proteins (α-Actinin-1/*ACTN1,* cofilin-1/*CFL1*),[24] and barbed-end

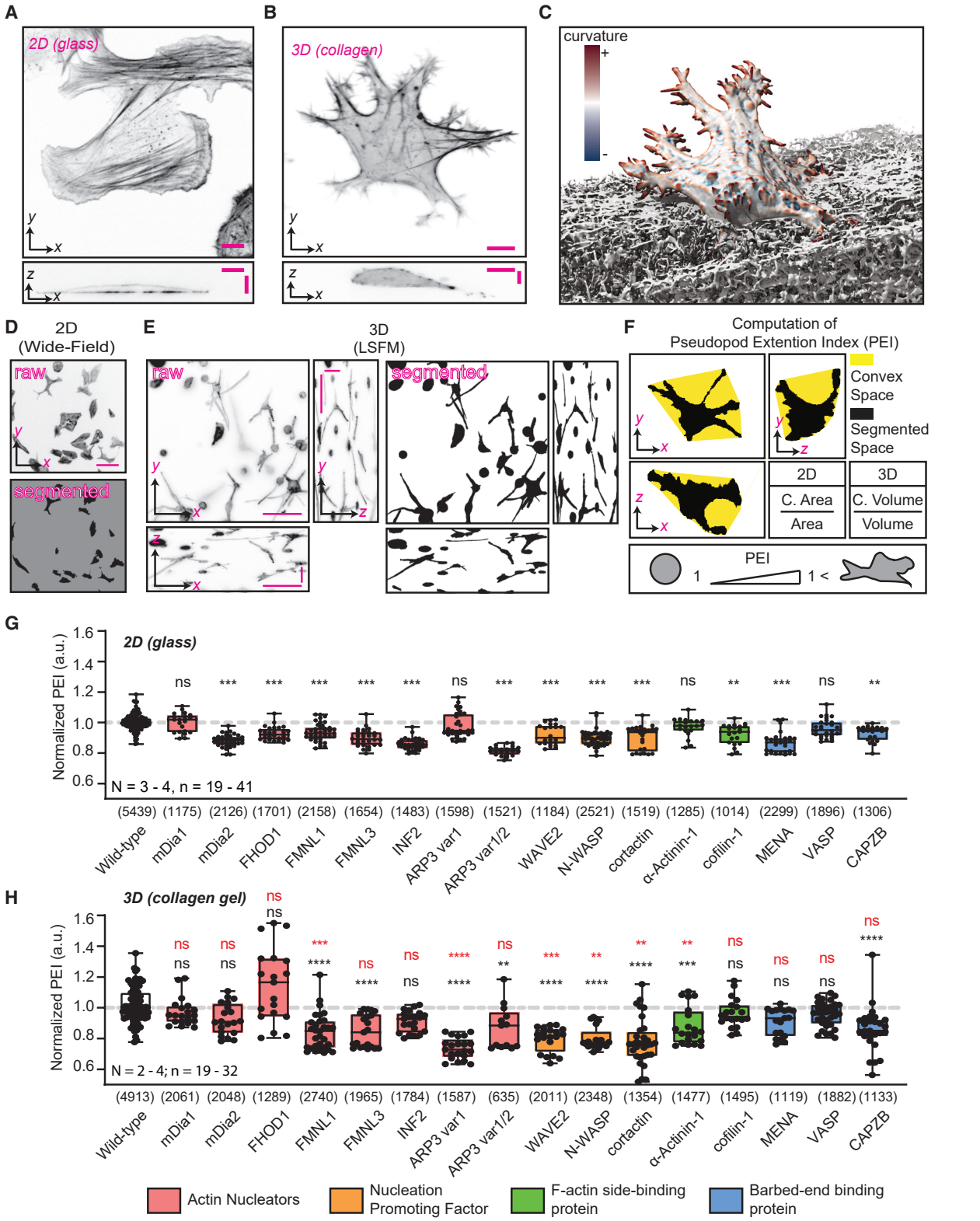

(legend on next page)

regulators (CapZβ/*CAPZB,* MENA/*ENAH,* VASP/*VASP*).[25] Arp3 has previously been reported to have two transcript variants, with alternating transcription initiation sites.[26] Therefore, we designed two independent guide RNAs (gRNAs): one which targets the exon only present in variant 1 (var1), the longest Arp3 variant, and another gRNA that targets a common exon region in both variants 1 and 2 (var1/2). We then generated two distinct Arp3 KO cell lines; an Arp3 var1 KO, and an Arp3 var1/2 KO (Figure S1A). None of the KOs caused noticeable cell growth defects under standard culture conditions, and all KOs were confirmed at the protein level (Figure S1B).

We first measured the degree of pseudopod extension on planar surfaces. Cells were seeded on thin collagen-coated (2 μg/mL) glass coverslips and allowed to adhere and spread for 16 h. To quantify the differences between cell morphologies of different knockouts, we segmented individual cells based on fluorescent F-actin staining and computed the ratio between the area of the convex hull embedding the entire cell perimeter and the segmented cell area as an overall index of pseudopod extension (Figures 1D–1F), i.e., the inverse of the "solidity" parameter.[27] Cells with a non-polarized round morphology will have a pseudopod extension index (PEI) close to 1. As cells polarize and extend protrusions the index monotonically increases without bounds (Figure 1F). These analyses revealed that most knockouts caused mild but significant pseudopod defects compared to the wildtype control cell population (Figure 1G). The exception to this was mDia1, α-Actinin-1, VASP, and Arp3 var1, which all showed no shift of the PEI relative to wild-type cells. We interpreted the lack of pseudopod defects in the Arp3 var1 KO cells as the result of residual expression of the Arp3 var2 protein (Figure S1A), which would maintain sufficient Arp2/3 activity for pseudopod formation. Indeed, Arp3 var1/2 KO cells, which is fully devoid of Arp3, showed the strongest pseudopod defects, stronger than defects of any Arp2/3 NPFs. In line with our interpretation that Arp3 var1 KO cells retain some Arp2/3 function, Arp3 var1 KO cells but not Arp3 var1/2 KO cells still showed sensitivity toward the Arp2/3 complex inhibitor CK-666 (Figure S1C).[28] Detailed high-resolution time-lapse analysis further indicated that Arp3 var1 KO cells exhibited a subtle defect in protrusion dynamics as determined by an increase in overall protrusion persistence (Figures S1D and S1E).

Next, we embedded the cells in reconstituted 3D collagen I gels (3 mg/mL; Figure 1H) and studied the effects of ABP KOs on multipolar pseudopod formation. In these experiments, cells were allowed to spread in the gel for 16 h prior to fixation, F-actin staining, and imaging. Analogous to the 2D quantification approach, we segmented individual cells in the acquired 3D image stacks and computed the PEI as a ratio between convex volume and the segmented cell volume in 3D (Figures 1E and 1F). As in 2D, mDia1 and VASP KOs showed no defects (Figure 1H) suggesting that these two ABPs are not directly implicated in pseudopod formation. For most ABP KOs with a defect in 2D, the defects in 3D tended to be more severe (Figure 1H, red asterisks). This suggests that anomalies in ABP functions are more readily tolerated in 2D, probably because protrusion extension on a flat substrate is molecularly less demanding. The exceptions to this trend were mDia2, INF2, cofilin-1, and MENA. Whereas their KO showed some pseudopod defects in 2D (Figure 1G), they did not affect the multipolar pseudopods in 3D (Figure 1H).

The strongest amplification of pseudopod defects when switching from 2D to 3D was observed for KOs targeting the Arp2/3 complex-associated branched actin network machinery, including Arp3 var1, Wave2, N-WASP, and cortactin. The Arp3 var1/2 KO cells continued to show pseudopod defects in 3D. Most strikingly, while Arp3 var1 KO cells displayed a heterogeneous PEI distribution and were not significantly affected in 2D (Figure 1G), these same cells showed the strongest decrease in PEI of all tested KO comparisons (Figure 1H). This was further confirmed by a second KO line generated using an independent guide RNA targeting sequence. (Figures S1F–S1I).

Dendritic actin network is required for pseudopod extension in soft environments

Acute inhibition of Arp2/3 activity using CK-666 resulted in similar differential pseudopod defects between 2D and 3D (Figures 2A–2D): In 2D, inhibition led to a heterogeneous response in pseudopod formation, which overall was insignificant when compared to an unperturbed control cell population. In 3D, inhibition of Arp2/3 activity caused a major deficiency in pseudopod formation. The sensitivity of these pseudopod defects to the cell culture conditions were reproduced in an untransformed human epithelial cell line (Figure S2). Together, these results highlight the essential contribution of Arp2/3 actin nucleating activity for multipolar pseudopod extension in 3D, while in 2D, minimal Arp2/3 activity is sufficient for pseudopod formation.

The differences we observed among the ABP KO responses between 2D and 3D cultures may originate from alterations in

Figure 1. Actin binding proteins regulate cell pseudopod extension differentially in cells cultured on 2D substrates and in a 3D matrix

(A) U2OS cells display a flat morphology on thin (2 μg/mL) collagen-coated glass coverslips.

(B) U2OS cells embedded in reconstituted collagen gels (3 mg/mL) display complex mixture of branched protrusions. (A and B) Cells were stained with fluorescent phalloidin and images were taken using light-sheet fluorescent microscope (LFSM),[9] and are representative from three experiments. Scale bars, 10 μm.

(C) Cells rendered in 3D using ChimeraX with the collagen environment partially removed to reveal the cell morphology.[10] Pseudopods are evident as regions of high curvature.

(D and E) Examples of cell segmentations (D) in 2D and (E) in 3D (shown as maximal intensity projections (MIP). Scale bars, 100 μm.

(F) Computation of pseudopod extension index (PEI) defined by the ratio between convex space and segmented space (space: area for 2D and volume for 3D). Cells with a PEI of 1 are convex and lack detectable protrusions. The index monotonically increases as cells become more protrusive and branched.

(G and H) Quantitation of cell pseudopod extensions (G) in 2D and (H) in 3D. All statistical testing was performed in comparison to the wild-type (black asterisks). Statistical comparison of the distribution of PEI between 3D and 2D are denoted with red asterisks. All data were collected from at least three independent experiments (N) except for ARP3 var1/2 in (H), $N = 2$. Each data point represents the median PEI of all cells within one image field of view (n), normalized to the mean PEI value of the wild-type control population. Total number of quantified individual cells are indicated in brackets under the graph, but not used to compute any statistics. Boxplots: Min/Max. Kruskal-Wallis test: ns = not significant, $^{**}p \leq 0.01$, $^{***}p \leq 0.001$, $^{****}p \leq 0.0001$.

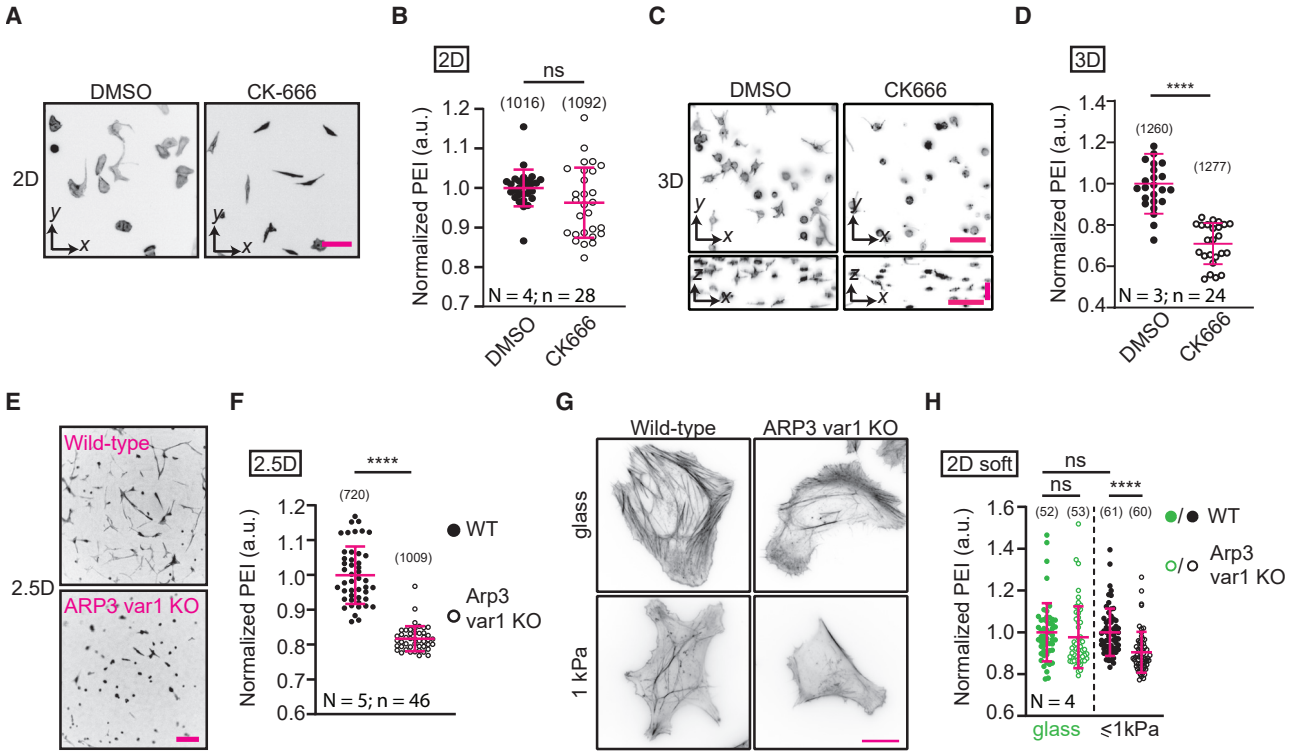

Figure 2. Arp2/3 complex-nucleated dendritic actin network is required for pseudopod extension in soft ECM environments

(A–D) Polymerization of the dendritic actin network is required for pseudopod extension in 3D, but not in 2D. (A and B) Cells were seeded on thin collagen-coated coverslips and treated with Arp2/3 inhibitor CK-666 for 1 h, and subsequently fixed, stained for F-actin, imaged and quantified as described in STAR Methods. PEI is normalized to DMSO control. (C and D) Collagen-embedded cells were treated overnight with Arp2/3 inhibitor CK-666. Cells were analyzed as in A, B, and normalized to DMSO control.

(E and F) Arp2/3 complex is required for pseudopod extension on top of soft 2D collagen gels (e.g., 2.5D). Cells were seeded on the surface of pre-polymerized collagen gel (3 mg/ml) and the PEI was computed as in (B). Data are normalized to wild-type control.

(G and H) Arp2/3 complex is required for pseudopod extension on soft substrates. Cells were seeded on soft silicone substrates ranging from 0.7–1.0 kPa in stiffness and PEI was quantified. For (B), (D), (F), (H), all data were collected from three to five independent experiments (N). Each data point represents the median PEI of all cells within one image field of view (n), except for (H), where each point represents a single cell from independent high-magnification images. Total number of individual cells are indicated in brackets. Data are shown as mean ± s.d. Kruskal-Wallis test: ns = not significant, $^{****}p \leq 0.0001$. Scale bars are 100 μm for (A), (C), (E) and 20 μm for (G).

ECM dimensionality, mechanical compliance of the substrate, or both. Cells on glass can extend pseudopodia in any direction and form integrin-mediated adhesions without geometric restriction. In contrast, cells in 3D must extend within a confined space and with the constraint that adhesions can form only in proximity to the collagen fibrils. Also, collagen gels are mechanically softer than collagen-coated glass (~0.2–0.6 kPa vs. >MPa[12,29]). Thus, we asked whether the fibrillar 3D geometry or the stiffness of the ECM was responsible for Arp2/3-dependent pseudopod extensions in 3D. To address this, we seeded wild-type and Arp3 var1 KO cells on top of a pre-polymerized collagen gel (2.5D), altering the confined geometry while minimally changing the stiffness and fibrillar architecture of the ECM in 3D. Under these conditions, Arp3 var1 KO cells continued to display a pseudopod defect relative to the wild-type cells (Figures 2E and 2F). Hence, the increased compliance and the fibrillar architecture of the ECM in 2.5D appeared to be sufficient to reproduce the pseudopod defects induced by Arp3 var1 KO or pharmacological inhibition of Arp2/3 activity in 3D.

To test whether the fibrillar collagen architecture is the main factor to impede pseudopods of Arp3 var1 KO and CK-666-inhibited cells, we used collagen-coated (2 μg/mL) and silicone-based 2D substrates with defined stiffnesses in the range 0.7–1 kPa. These substrates resemble the surfaces of collagen-coated 2D glass slides, i.e., they lack collagen fibrils, but they have a stiffness nearing that of collagen gels.[29] On these substrates, the Arp3 var1 KO cells consistently displayed reduced PEI compared to the wild-type cells (Figures 2G and 2H). However, the overall reduction in PEI was less compared to that of cells seeded on 2.5D or in 3D (Figures 2D–2F). These results suggest that architectural features in addition to the stiffness of the ECM attenuate pseudopod extensions of Arp3 var1 KO cells.

Arp2/3 complex regulates cell-matrix adhesions in a stiffness-dependent manner

In view of the pseudopod defects of Arp3 var1 KO and CK-666-inhibited cells on soft substrates, we hypothesized that Arp2/3's critical function on compliant ECM may relate to the contribution

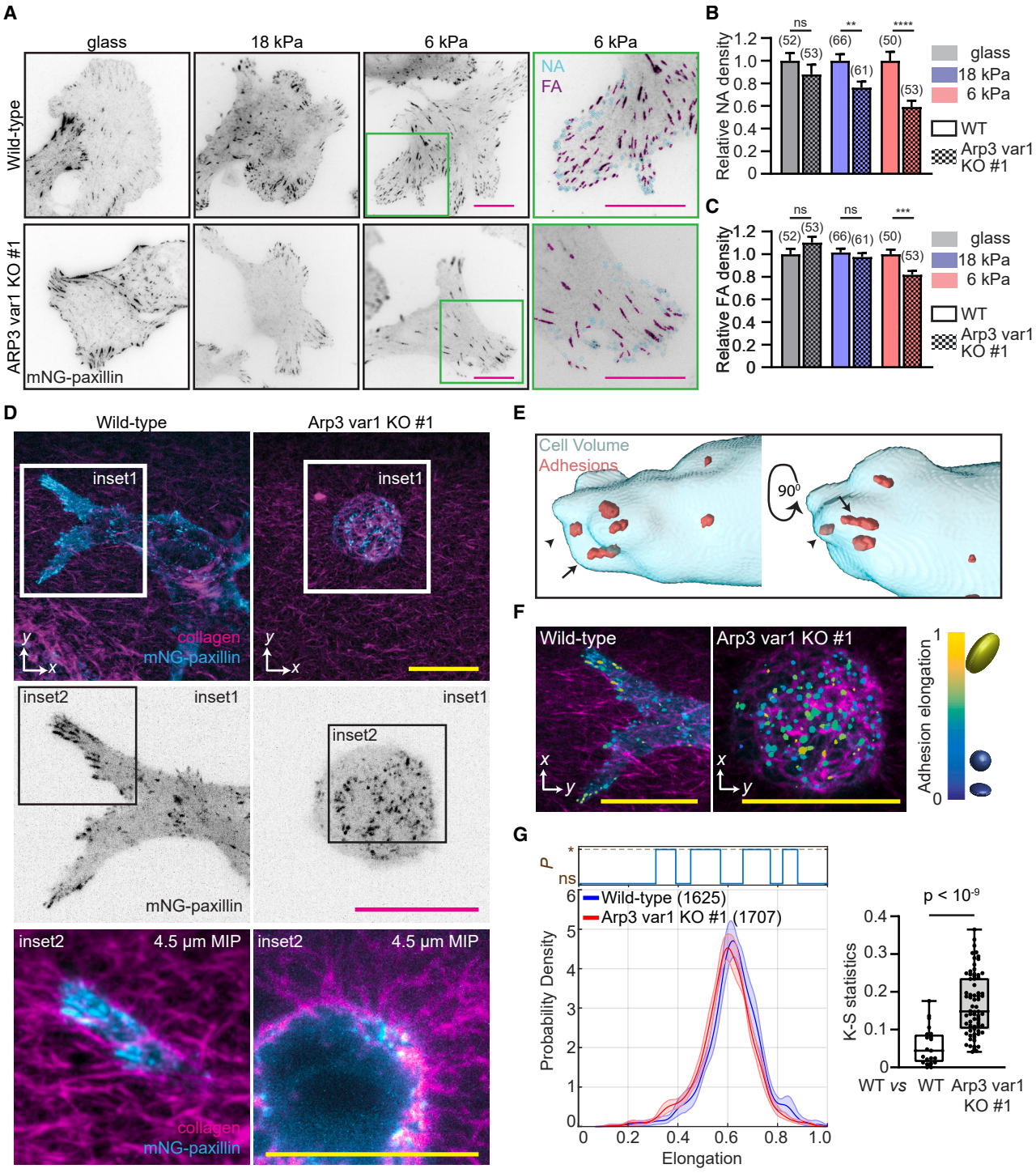

Figure 3. Arp2/3 complex regulates cell-matrix adhesions in a stiffness-dependent manner

(A) Focal adhesions in cells seeded on collagen-coated glass or silicone substrates were imaged using TIRF. Adhesions, visualized with mNeonGreen-paxillin were classified into nascent adhesions (NA) or mature focal adhesions (FA) using previously described software[32] (STAR Methods).

(B and C) Differential effects of Arp3 var1 KO on NA and FA density, with increasing sensitivity on softer substrates. (B) NA and (C) FA densities (number/cell area). Data were collected from four independent experiments (N) and shown as mean ± s.e.m. Number of individual cells are indicated in brackets. t-test: ns = not significant, $^{**}p \leq 0.01$, $^{***}p \leq 0.001$, $^{****}p \leq 0.0001$.

(D) Arp3 var1 KO cells have adhesion defects in 3D. MIPs of adhesions (cyan; mNeonGreen-paxillin) of cells embedded in AlexaFluor 568-labeled collagen (magenta) are shown. Inset1 illustrates elongated and non-elongated adhesions. Inset2 shows a 4.5 µm MIP of protruding areas of a cell.

(legend continued on next page)

of branched actin networks to nascent and focal adhesions formation (NAs and FAs, respectively[22,30]). To test whether adhesion formation on soft substrates relies on Arp2/3 activity, we imaged the adhesion protein paxillin in wild-type and Arp3 var1 KO cells with total internal reflection fluorescence (TIRF)-compatible 2D soft substrates[31] and used previously described computer software to distinguish NAs from mature FAs.[32] These analyses showed that, although statistically insignificant, Arp3 var1 KO cells had less NAs per cell area on stiff glass substrates compared to WT cells. This difference became significant on increasingly softer substrates (Figures 3A–3C). In contrast, Arp3 var1 KO cells showed similar levels of mature FAs, with only a marginal decrease at lower stiffness (Figures 3A–3C). Thus, while knock-out of Arp3 var1 generated an adhesion defect on 2D substrates, the remnant Arp2/3 activity in these cells seemed sufficient to support the initial cell adhesion formation necessary for pseudopod extension. The differential in pseudopod defect between Arp3 var1 KO and Arp3 var1/2 KO cells would therefore be attributed to the remaining presence vs. complete absence of Arp2/3 activity in the early phases of pseudopod extension. To test this, we seeded the Arp3 var1 KO cells in the presence of CK-666 (O/N). Quantification showed that the Arp3 var1 KO cells had pseudopod defects even stronger than cells treated with CK-666 after attachment (Figures S3 and S1C). Notably, the degree of the defect was similar to that of Arp3 var1/2 KO cells, which are fully devoid of Arp2/3 activity (Figure S3; Figure 1G). Thus, Arp2/3 activity contributes to NA formation, and this activity becomes increasingly indispensable as cells experience softer substrate stiffness.

We then hypothesized that the deficiency in pseudopod extension observed for Arp3 var1 KO cells in 3D relates to defects in adhesion formation as well. We evaluated this by imaging paxillin in collagen-embedded cells using light-sheet microscopy. Because wild-type cells extend more pseudopods than Arp3 var1 KO cells and occupy a greater volume, the NA density per area or volume for Arp3 var1 KO cells is inflated (Figure 3D). Instead, using customized tracking software[33] (STAR Methods), we measured the elongation of adhesion-like structures as a proxy for the level of engagement of an adhesion with a collagen fiber (Figures 3D–3G). These analyses showed that wild-type cells have significantly more elongated adhesion-like structures than Arp3 var1 KO cells (Figures 3F and 3G), again pointing at a defect in cell-substrate interactions under Arp3 var1 KO conditions. In 2D, defects in Arp2/3-dependent adhesion formation pathways are compensated by alternative pathways in an already overall saturated density of adhesions. In 3D, where adhesion formation is rate-limited by the fibrillar topology of extracellular ligands,[11,34] such defects translate into failure of pseudopod extension.

The Arp2/3-vinculin hybrid complex is required for pseudopod extension in 3D

Next, we considered the underlying molecular mechanisms for Arp2/3 in adhesion formation in 3D or on compliant substrates. The data thus far suggest that the Arp2/3-mediated branched actin network offers specific benefits to the adhesion assembly process. To date, FAK/*PTK2*, vinculin/*VCL*, and kindlin-2/*FERMT2* are the sole adhesion molecules known to directly interact with the Arp2/3 complex.[19–22] Although the contribution of their interaction to pseudopod formation has been studied extensively on 2D substrates, much less is known about their contribution to pseudopod formation in 3D environments. To evaluate this, we generated KOs of FAK, kindlin-2, and vinculin. KOs of kindlin-2 and vinculin showed marked pseudopod defects in 3D collagen matrices, while FAK KO significantly increased the protrusive ability of cells (Figures 4A and 4B; Figures S4A–S4C). Further analysis revealed that kindlin-2 KO cells also had a prominent pseudopod defect in 2D, while vinculin KO cells showed only a modest defect that is comparable to that of Arp3 var1 KO cells (PEI means of 0.93 ± 0.05 vs. 0.98 ± 0.08, respectively. Figure S4C; Figure 1G). We therefore concluded that kindlin-2's primary function in adhesion formation cannot be compensated in 2D, as it is essential for the surface expression and activation of integrins.[35–37] This role likely has more profound, Arp2/3-independent effects on adhesion formation. Accordingly, we turned our attention to vinculin as its KO phenotype showed the same sensitivity to 2D vs. 3D environments as that of Arp3 var1 KO and CK-666-inhibited cells.

Vinculin is a mechanoresponsive focal adhesion protein,[3,38–40] which is required for persistent migration through 3D collagen gels in a myosin II-independent manner.[41] The proline-rich linker region of vinculin was shown to bind and recruit the p34-ARC subunit of the Arp2/3 complex, and this interaction was suggested to couple adhesion formation with Arp2/3 and lamellipodial dynamics.[21] Later, independent experiments indicated that vinculin enters into a complex with the nucleation active core of the Arp2/3 consisting of Arp2, Arp3, p21-ARC, and p34-ARC.[22,42] Importantly, this hybrid Arp2/3-vinculin complex was shown to be in a mutually exclusive existence to the canonical heptameric Arp2/3 complex. We conjecture that the p34-ARC-vinculin interaction described by DeMali et al., and the hybrid Arp2/3-vinculin complex identified by Chorev et al., are the same. Functionally, this hybrid Arp2/3-vinculin complex has not been highlighted as a central feature of adhesion formation,

(E) 3D rendering examples of elongated (arrow) and non-elongated (arrowhead) focal adhesions in 3D.
(F) Arp3 var1 KO cells have reduced elongated adhesions in 3D. The degree of elongation of adhesions in 3D was quantified with customized 3D tracking software (STAR Methods). Adhesions with an elongation index of 0 are fully round. The index increases as adhesions become increasingly elongated. Adhesions are pseudocolored according to the elongation index.
(G) *left*, Probability density distribution of adhesion elongation index. Shaded areas represent 95% confidence intervals of the mean adhesion elongation. Statistical significance (*P*) (ns = not significant; * = $p < 0.05$) of the difference between the elongation index distributions is assessed for 100 non-overlapping 1% quantiles in the elongation range of [0 … 1], is determined by t-test. Total of 1625 and 1707 individual adhesions for WT and Arp3 var1 KO cells, respectively were analyzed, as indicated in brackets. *right*, Distributions of K-S statistics of the difference in elongation index distributions between either individual wild-type (WT) cells or between WT and Arp3 var1 KO cells (7 cells for WT and 10 cells for Arp3 var1 KO from a representative experiment out of two independent experiments) further confirms the significance of adhesion elongation differences between these two conditions. All scale bars, 20 μm.

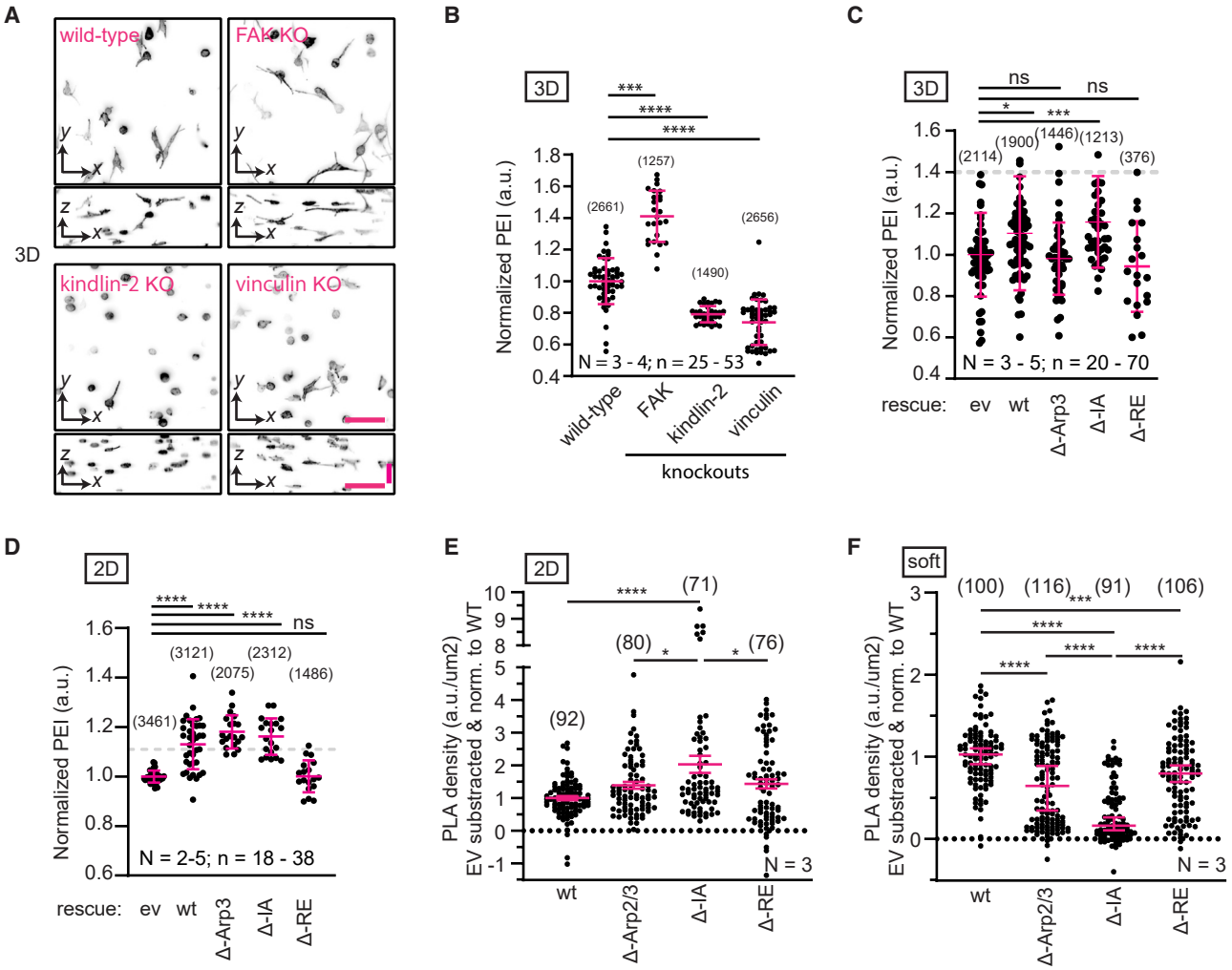

Figure 4. The Arp2/3-vinculin hybrid complex is required for pseudopod extension in 3D

(A and B) Vinculin and kindlin-2, but not FAK knockout U2OS cells have spreading defects in 3D. Cells embedded in collagen gels were stained for F-actin, imaged and quantified as described in STAR Methods. PEI is normalized to wild-type control. Data are shown as mean ± s.d. Kruskal-Wallis test: $^{***}p \leq 0.001$, $^{****}p \leq 0.0001$

(C) Direct Arp2/3-binding by vinculin is required for vinculin function during pseudopod extension in 3D. Vinculin KO cells were reconstituted with empty vector (ev), wild-type (wt), Arp3-binding mutant (Δ-Arp3) or Actin-binding mutants (Δ-IA or Δ-RE) in full-length vinculin. PEI values are normalized to the mean of the ev-distribution. Gray dotted line designates the spread levels of wild-type U2OS cells. Seven data points are outside the y axis limit, and the full graph is presented in Figure S4E. Data are shown as mean ± s.d. Kruskal-Wallis test: ns = not significant, $^{*}p \leq 0.05$, $^{***}p \leq 0.001$.

(D) Arp2/3-binding by vinculin is not essential for vinculin function during pseudopod extension in 2D. Vinculin KO cells were reconstituted with empty vector (ev), wild-type (wt) or indicated vinculin mutants (Arp3-binding mutant (Δ-Arp3), Actin-binding mutants (Δ-IA or Δ-RE)). PEI values are normalized to the mean of the ev-distribution. Gray dotted line designates the spread levels of wild-type U2OS cells. All vinculin constructs except the Δ-RE mutant were able to restore pseudopod formation of the vinculin KO cells comparable to that of wild-type U2OS cells. All data were collected from two to five independent experiments (N) and are shown as mean ± s.d. Each data point represents the median of the PEI of all cells within one image field of view (n) and normalized to the mean of the ev-distribution. Total number of quantified individual cells are indicated in brackets, but not used to compute any statistics. Kruskal-Wallis test: ns = not significant, $^{*}p < 0.05$, $^{**}p \leq 0.01$, $^{***}p \leq 0.001$, $^{****}p \leq 0.0001$.

(E) Hybrid Arp2/3-vinculin complex formation is not abrogated in 2D. p34-ARC-vinculin PLA density was detected in cells seeded on collagen-coated glass coverslips, background subtracted (see STAR Methods) and normalized to wild-type cells (wt). Each data point represents a cell. Data were collected from three independent experiments (N). Total number of quantified cells are indicated in brackets. Mean ± s.e.m. One-way ANOVA: $^{*}p < 0.05$, $^{****}p \leq 0.0001$.

(F) Formation of the hybrid Arp2/3-vinculin complex is sensitive to the extracellular environment. p34-ARC-vinculin PLA densities were analyzed as in (E) but from cells seeded on soft substrate (~8 kPa). Each data point represents a cell. Data were collected from three independent experiments (N). Total number of quantified cells are indicated in brackets. Mean ± s.e.m. One-way ANOVA: $^{***}p \leq 0.001$, $^{****}p \leq 0.0001$.

as vinculin deficient of Arp2/3-binding had minimal effects on cell adhesion and pseudopod extension in 2D.[21] Rather, the common models of adhesion formation consider vinculin's direct binding to actin filaments as an essential component for the stabilization of NAs and maturation into FAs.[38,40,43,44] Given our observation that both Arp2/3 activity and vinculin are essential

for efficient pseudopod extension in 3D, we hypothesized that the hybrid Arp2/3-vinculin complex activity may constitute a critical feature for multipolar pseudopodial projections in 3D that is dispensable in 2D. To distinguish the contributions of the hybrid Arp2/3-vinculin complex from that of vinculin-actin interaction during 3D pseudopod extension, we reconstituted vinculin KO cells with (1) wild-type vinculin, (2) a P878A vinculin mutant deficient in Arp2/3 complex-binding (Δ-Arp2/3,[21]), and two actin-binding and bundling deficient mutants mapped to alternative actin-interacting surfaces on the vinculin tail, i.e., (3) the I997A (Δ-IA,[41,43]), and (4) the R1047E (Δ-RE,[45,46]) mutants (Figure S4D). We then examined the PEI values of these cell types in 3D relative to the PEI values of KO cells transfected with an empty vector control (Figures 4C and S4E). Vinculin KO cells reconstituted with wild-type vinculin were partially rescued for their pseudopod defects in 3D. In contrast, expression of the Δ-Arp2/3 and Δ-RE vinculin mutant failed to rescue the KO cells, whereas expression of the Δ-IA actin mutant rescued pseudopod defects to the level of cells reconstituted with wild-type vinculin.

This finding is rather remarkable in view of the rich literature, which defines —based on 2D experiments— vinculin's actin-binding as a central feature of adhesion formation and maturation.[43,47] Our own analysis confirmed that in 2D all mutants except the Δ-RE mutant rescued the pseudopod defects of vinculin KO cells (Figure 4D). Hence, Arp2/3-vinculin interactions are non-essential for protrusion extension with cells cultured on stiff glass substrates, but they seem critical for the same process in 3D. In line with the functional readout through protrusion extension, proximity ligation assay (PLA)[48] between p34-ARC and vinculin suggested that all tested mutants retained hybrid Arp2/3-vinculin complex formation in 2D (Figure 4E; Figure S5A). In stark contrast, in cells seeded on soft substrates (∼8 kPa), the hybrid Arp2/3-vinculin complex formation was strongly attenuated in the Δ-Arp2/3 mutant rescue (Figure 4F). To a lesser extent the interaction was also reduced in the Δ-RE mutant rescue and, to our surprise, almost completely abrogated in the Δ-IA mutant (Figure 4F). Pull-down experiments showed that all mutants except the Δ-Arp2/3 mutant retained interaction with the Arp2/3 complex (Figure S5B). These data collectively suggest that the Arp2/3-vinculin interactions are subject to a complex, substrate-dependent regulation in cells, and depend on the crosstalk between the two actin-interacting surfaces on vinculin,[46] in addition to other vinculin-interacting partners.[49]

DISCUSSION

Our results highlight the critical differences between pseudopods on flat, stiff 2D substrates, which has been the workhorse for the analysis of cytoskeleton and adhesion function by high-resolution microscopy and multipolar pseudopod projections in 3D collagen or on compliant 2D substrates. We show that the hybrid Arp2/3-vinculin complex, which is perfectly dispensable in 2D, is an essential component for pseudopod formation in 3D. Clearly, cytoskeleton architecture and adhesions are cellular features that are particularly vulnerable to cell culture artifacts. Our results suggest that pseudopod extension in 2D can operate on either one of two interchangeable pathways implicating Arp2/3: a pathway in which the canonical heptameric Arp2/3 acts as the nucleator of branched F-actin, promoting membrane protrusion, and a pathway in which the hybrid Arp2/3-vinculin complex promotes the synergistic assembly of NAs and branched actin. In 3D or 2D soft substrate surrogates for fibrillar ECM, where the chances for establishing mechanically stable links between ECM and cytoskeleton is reduced, pseudopod extension depends on the efficient coupling of nascent adhesions with the actin branches. The coupling seems controlled in a complex fashion in crosstalk with vinculin's canonical direct coupling to actin, which has been mostly studied in the context of maturing adhesion. *In vitro*, the actin-interacting vinculin tail (Vt) adopts a five-helix (H1-H5) bundle fold with a small 5 amino acid C-terminal extending hairpin. In the presence of F-actin, Vt undergoes homodimerization through undocking of the H1 helix and bundles F-actin.[50–52] The removal of the C-terminal hairpin (ΔC5) abrogated bundling but not F-actin binding.[52,53] Biochemically, the ΔC5 vinculin mutant showed reduced interaction with the Arp2/3 and surprisingly no enrichment of actin. Paradoxically, when overexpressed in cells, the ΔC5 mutant increased cell spreading beyond cells expressing wild-type vinculin,[54] indicating that the functions of vinculin's interaction with actin in cell adhesion remains to be fully elucidated. In light of our work, both Δ-IA and Δ-RE mutants have different functional and biochemical consequences in soft environments (Figures 4C–4E), and this may pertain to how the two actin-interacting surfaces act in tandem to enable the homodimerization of the Vt, F-actin bundling and Arp2/3 interaction.[46,55]

Whereas the weak rescue of pseudopod extension by the Δ-RE vinculin mutant in 3D, matching the low level of rescue by the Δ-Arp2/3 mutant, is aligned with a reduction of Arp2/3-vinculin complex formation, how the actin-binding and bundling deficient Δ-IA mutant, almost completely devoid of forming a complex with Arp2/3, still partially rescued pseudopod formation in 3D remains an important subject that warrants future investigation. Critically, these experiments must rely on a 3D cell culture format, both for biochemistry and functional readouts. On a 2D glass or tissue culture plastic substrate, where links between actin and ECM can be generated abundantly, a less coordinated interaction of vinculin with Arp2/3 and actin is sufficient to provide the mechanical anchorage necessary for pseudopod extension. Altogether, these data highlight how experiments on stiff, planar substrates may conceal critical cytoskeletal architectures that are essential for the establishment of cellular morphogenesis in 3D.

Limitations of the study

This work provides insights of the differential roles Arp2/3 – vinculin binding plays on 2D versus 3D substrates and, more broadly, raises questions regarding the sensitivity of the relationship between ABPs and pseudopod extensions to geometrically and/or mechanically variable environments. However, we refrain from claiming universality of these findings. Our data stems from one primary cell line. Additionally, our analytical approach to phenotyping is optimized for higher throughput, focusing on a single, gross morphological effect that is measured in fixed cells. Future studies utilizing high-resolution

and timelapse imaging are necessary to uncover more subtle defects not explicitly documented here.

Using a series of reconstitution assays, we revealed that Arp2/3-vinculin interaction is required for pseudopod extensions, specifically in soft and 3D environments, but dispensable in 2D on glass. Biochemically, the Δ-Arp2/3 was the only mutant with reduced Arp2/3 interaction. In contrast, PLA analysis between p34-ARC and vinculin in reconstituted cells seeded on soft substrates showed that Δ-Arp2/3 and Δ-RE mutants showed reduced signal, whereas Δ-IA was almost completely abrogated. Functionally, Δ-Arp2/3 and the Δ-RE mutants failed to rescue pseudopod formations in 3D, whereas wild-type and Δ-IA successfully rescued pseudopod formation in 3D.

The discrepancy between functional, biochemical, and PLA results likely arises from the nature of the PLA method, which detects protein interaction based on proximity, including indirect interactions. This may explain the positive PLA results between p34-ARC and vinculin in 2D conditions where Arp2/3 and vinculin occupy a co-regulated space during cell spreading. For 3D data, additional confirmation of Arp2/3-vinculin interactions in 3D would be needed to gain full clarity on their functional implications.

Given that vinculin may undergo additional structural changes in cells, real-time interaction analysis in 3D using fluorescence resonance energy transfer (FRET)-based probes could provide additional clarity. Such an approach may also inform on the cascade of Arp2/3 activation, hybrid complex formation with vinculin, and the engagement of the Arp2/3-vinculin complex with collagen fibers in 3D.

RESOURCE AVAILABILITY

Lead contact

Requests for further information and resources should be directed to and will be fulfilled by the lead contact, Tadamoto Isogai (Tadamoto.Isogai@UTSouthwestern.edu).

Materials availability

All unique/stable reagents generated in this study are available from the lead contact with a completed materials transfer agreement.

Data and code availability

All data reported in this paper will be shared by the lead contact upon request. Code is available under https://github.com/DanuserLab/Isogai-ARP23-Paper-2025. Any additional information required to reanalyze the data reported in this paper is available from the lead contact upon request.

ACKNOWLEDGMENTS

We thank Dr. Dana Reed and Ms. Meghan Doyal (UT Southwestern Medical Center) for their logistical support, and Dr. Jungsik Noh for helpful discussion on functional data analysis and statistical testing. Funding for this work was provided by grants from the National Institutes of Health (F32GM117793 to K.M.D., F32GM116370 and K99GM123221 to M.K.D., R33CA235254 to R. F., and R35GM136428 to G.D.). The content of the manuscript is solely the responsibility of the authors and does not represent the official views of the funding agencies. This research was supported in part by the computational resources provided by the BioHPC facility located in the Lyda Hill Department of Bioinformatics, UT Southwestern Medical Center, TX, and the UT Southwestern Quantitative Live Microscopy Core Facility, a Shared Resource of the Harold C. Simmons Cancer Center, supported in part by an NCI Cancer Center Support Grants, 1P30 CA142543-01.

AUTHOR CONTRIBUTIONS

Conceptualization: T.I. and G.D.; methodology: T.I., K.M.D., K.B., S.P.R., and N.M.; investigation: T.I., K.M.D., and E.V.A.; formal analysis: T.I., K.M.D., P.R., and S.J.H.; resources: B.-J.C. and R.F.; visualization: P.R. and M.K.D.; writing – original draft: T.I., K.M.D., and G.D.; writing – review and editing: T. I. and G.D.; funding acquisition: K.M.D., M.K.D., and G.D.; supervision and project administration: T.I. and G.D.

DECLARATION OF INTERESTS

Current institutional affiliations of authors not listed on the title page: P.R., CNRS and Institut Fresnel, Marseilles, France; E.V.A., Bioengineering, John Hopkins University, Baltimore, MD; M.K.D. University of Minnesota, Minneapolis, MN; N.M. Thermo Fisher Scientific.

K.M.D. and R.F. hold a patent for the axially scanned light-sheet microscope that is currently licensed by Intelligent Imaging Innovations, Inc. and subsequently sub-licensed by Life Canvas Technologies but do not have any investment interests or financial stakes in these companies. K.M.D. has an investment interest in Discovery Imaging Systems, LLC. G.D. is a member of the Board of Glencoe Software, Inc.

STAR★METHODS

Detailed methods are provided in the online version of this paper and include the following:

- KEY RESOURCES TABLE
- EXPERIMENTAL MODEL AND STUDY PARTICIPANT DETAILS
  - Cell lines and culture conditions
- METHOD DETAILS
  - Plasmids
  - Generation of knockout cell lines
  - CRISPR knockout validation
  - Two-dimensional PEI assay
  - Large field-of-view LSFM (IFOV-LSFM)
  - Sample preparation for 3D imaging
  - Pharmacological perturbations
  - Analysis of protrusion dynamics in 2D
  - 2D TIRF imaging of focal adhesions
  - High-resolution focal adhesion imaging in 3D
  - Pull-down assay
  - p34-ARC-vinculin proximity ligation assay (PLA)
- QUANTIFICATION AND STATISTICAL ANALYSIS
  - Two-dimensional PEI analysis
  - Three-dimensional PEI analysis
  - Focal adhesions analysis in 2D
  - Focal adhesion characterization in 3D
  - p34-ARC-vinculin PLA analysis
  - Statistical analysis

SUPPLEMENTAL INFORMATION

Supplemental information can be found online at https://doi.org/10.1016/j.isci.2025.112623.

Received: November 1, 2024
Revised: April 2, 2025
Accepted: May 6, 2025
Published: May 9, 2025

REFERENCES

1. Discher, D.E., Janmey, P., and Wang, Y.L. (2005). Tissue cells feel and respond to the stiffness of their substrate. Science *310*, 1139–1143. https://doi.org/10.1126/science.1116995.

2. Geiger, B., Bershadsky, A., Pankov, R., and Yamada, K.M. (2001). Transmembrane crosstalk between the extracellular matrix–cytoskeleton crosstalk. Nat. Rev. Mol. Cell Biol. *2*, 793–805. https://doi.org/10.1038/35099066.

3. Schiller, H.B., and Fässler, R. (2013). Mechanosensitivity and compositional dynamics of cell-matrix adhesions. EMBO Rep. *14*, 509–519. https://doi.org/10.1038/embor.2013.49.

4. Caswell, P.T., and Zech, T. (2018). Actin-Based Cell Protrusion in a 3D Matrix. Trends Cell Biol. *28*, 823–834. https://doi.org/10.1016/j.tcb.2018.06.003.

5. Pollard, T.D., and Cooper, J.A. (2009). Actin, a central player in cell shape and movement. Science *326*, 1208–1212. https://doi.org/10.1126/science.1175862.

6. dos Remedios, C.G., Chhabra, D., Kekic, M., Dedova, I.V., Tsubakihara, M., Berry, D.A., and Nosworthy, N.J. (2003). Actin binding proteins: regulation of cytoskeletal microfilaments. Physiol. Rev. *83*, 433–473. https://doi.org/10.1152/physrev.00026.2002.

7. Pollard, T.D., Blanchoin, L., and Mullins, R.D. (2000). Molecular mechanisms controlling actin filament dynamics in nonmuscle cells. Annu. Rev. Biophys. Biomol. Struct. *29*, 545–576. https://doi.org/10.1146/annurev.biophys.29.1.545.

8. Dominguez, R., and Holmes, K.C. (2011). Actin structure and function. Annu. Rev. Biophys. *40*, 169–186. https://doi.org/10.1146/annurev-biophys-042910-155359.

9. Dean, K.M., Roudot, P., Welf, E.S., Danuser, G., and Fiolka, R. (2015). Deconvolution-free Subcellular Imaging with Axially Swept Light Sheet Microscopy. Biophys. J. *108*, 2807–2815. https://doi.org/10.1016/j.bpj.2015.05.013.

10. Goddard, T.D., Huang, C.C., Meng, E.C., Pettersen, E.F., Couch, G.S., Morris, J.H., and Ferrin, T.E. (2018). UCSF ChimeraX: Meeting modern challenges in visualization and analysis. Protein Sci. *27*, 14–25. https://doi.org/10.1002/pro.3235.

11. Fraley, S.I., Feng, Y., Krishnamurthy, R., Kim, D.H., Celedon, A., Longmore, G.D., and Wirtz, D. (2010). A distinctive role for focal adhesion proteins in three-dimensional cell motility. Nat. Cell Biol. *12*, 598–604. https://doi.org/10.1038/ncb2062.

12. Doyle, A.D., Carvajal, N., Jin, A., Matsumoto, K., and Yamada, K.M. (2015). Local 3D matrix microenvironment regulates cell migration through spatiotemporal dynamics of contractility-dependent adhesions. Nat. Commun. *6*, 8720. https://doi.org/10.1038/ncomms9720.

13. Doyle, A.D., Petrie, R.J., Kutys, M.L., and Yamada, K.M. (2013). Dimensions in cell migration. Curr. Opin. Cell Biol. *25*, 642–649. https://doi.org/10.1016/j.ceb.2013.06.004.

14. Cukierman, E., Pankov, R., Stevens, D.R., and Yamada, K.M. (2001). Taking cell-matrix adhesions to the third dimension. Science *294*, 1708–1712. https://doi.org/10.1126/science.1064829.

15. Christensen, J.R., Homa, K.E., Morganthaler, A.N., Brown, R.R., Suarez, C., Harker, A.J., O'Connell, M.E., and Kovar, D.R. (2019). Cooperation between tropomyosin and alpha-actinin inhibits fimbrin association with actin filament networks in fission yeast. Elife *8*, e47279. https://doi.org/10.7554/eLife.47279.

16. Winkelman, J.D., Suarez, C., Hocky, G.M., Harker, A.J., Morganthaler, A. N., Christensen, J.R., Voth, G.A., Bartles, J.R., and Kovar, D.R. (2016). Fascin- and alpha-Actinin-Bundled Networks Contain Intrinsic Structural Features that Drive Protein Sorting. Curr. Biol. *26*, 2697–2706. https://doi.org/10.1016/j.cub.2016.07.080.

17. Campellone, K.G., and Welch, M.D. (2010). A nucleator arms race: cellular control of actin assembly. Nat. Rev. Mol. Cell Biol. *11*, 237–251. https://doi.org/10.1038/nrm2867.

18. Goley, E.D., and Welch, M.D. (2006). The ARP2/3 complex: an actin nucleator comes of age. Nat. Rev. Mol. Cell Biol. *7*, 713–726. https://doi.org/10.1038/nrm2026.

19. Serrels, B., Serrels, A., Brunton, V.G., Holt, M., McLean, G.W., Gray, C.H., Jones, G.E., and Frame, M.C. (2007). Focal adhesion kinase controls actin assembly via a FERM-mediated interaction with the Arp2/3 complex. Nat. Cell Biol. *9*, 1046–1056. https://doi.org/10.1038/ncb1626.

20. Bottcher, R.T., Veelders, M., Rombaut, P., Faix, J., Theodosiou, M., Stradal, T.E., Rottner, K., Zent, R., Herzog, F., and Fassler, R. (2017). Kindlin-2 recruits paxillin and Arp2/3 to promote membrane protrusions during initial cell spreading. J. Cell Biol. *216*, 3785–3798. https://doi.org/10.1083/jcb.201701176.

21. DeMali, K.A., Barlow, C.A., and Burridge, K. (2002). Recruitment of the Arp2/3 complex to vinculin: coupling membrane protrusion to matrix adhesion. J. Cell Biol. *159*, 881–891. https://doi.org/10.1083/jcb.200206043.

22. Chorev, D.S., Moscovitz, O., Geiger, B., and Sharon, M. (2014). Regulation of focal adhesion formation by a vinculin-Arp2/3 hybrid complex. Nat. Commun. *5*, 3758. https://doi.org/10.1038/ncomms4758.

23. Chesarone, M.A., DuPage, A.G., and Goode, B.L. (2010). Unleashing formins to remodel the actin and microtubule cytoskeletons. Nat. Rev. Mol. Cell Biol. *11*, 62–74. https://doi.org/10.1038/nrm2816.

24. Winder, S.J., and Ayscough, K.R. (2005). Actin-binding proteins. J. Cell Sci. *118*, 651–654. https://doi.org/10.1242/jcs.01670.

25. Shekhar, S., Pernier, J., and Carlier, M.F. (2016). Regulators of actin filament barbed ends at a glance. J. Cell Sci. *129*, 1085–1091. https://doi.org/10.1242/jcs.179994.

26. Abella, J.V.G., Galloni, C., Pernier, J., Barry, D.J., Kjær, S., Carlier, M.F., and Way, M. (2016). Isoform diversity in the Arp2/3 complex determines actin filament dynamics. Nat. Cell Biol. *18*, 76–86. https://doi.org/10.1038/ncb3286.

27. Wu, P.H., Phillip, J.M., Khatau, S.B., Chen, W.C., Stirman, J., Rosseel, S., Tschudi, K., Van Patten, J., Wong, M., Gupta, S., et al. (2015). Evolution of cellular morpho-phenotypes in cancer metastasis. Sci. Rep. *5*, 18437. https://doi.org/10.1038/srep18437.

28. Nolen, B.J., Tomasevic, N., Russell, A., Pierce, D.W., Jia, Z., McCormick, C.D., Hartman, J., Sakowicz, R., and Pollard, T.D. (2009). Characterization of two classes of small molecule inhibitors of Arp2/3 complex. Nature *460*, 1031–1034. https://doi.org/10.1038/nature08231.

29. Bordeleau, F., Mason, B.N., Lollis, E.M., Mazzola, M., Zanotelli, M.R., Somasegar, S., Califano, J.P., Montague, C., LaValley, D.J., Huynh, J., et al. (2017). Matrix stiffening promotes a tumor vasculature phenotype. Proc. Natl. Acad. Sci. USA *114*, 492–497. https://doi.org/10.1073/pnas.1613855114.

30. Choi, C.K., Vicente-Manzanares, M., Zareno, J., Whitmore, L.A., Mogilner, A., and Horwitz, A.R. (2008). Actin and alpha-actinin orchestrate the assembly and maturation of nascent adhesions in a myosin II motor-independent manner. Nat. Cell Biol. *10*, 1039–1050. https://doi.org/10.1038/ncb1763.

31. Gutierrez, E., Tkachenko, E., Besser, A., Sundd, P., Ley, K., Danuser, G., Ginsberg, M.H., and Groisman, A. (2011). High refractive index silicone gels for simultaneous total internal reflection fluorescence and traction force microscopy of adherent cells. PLoS One *6*, e23807. https://doi.org/10.1371/journal.pone.0023807.

32. Han, S.J., Oak, Y., Groisman, A., and Danuser, G. (2015). Traction microscopy to identify force modulation in subresolution adhesions. Nat. Methods *12*, 653–656. https://doi.org/10.1038/nmeth.3430.

33. Roudot, P., Legant, W.R., Zou, Q., Dean, K.M., Isogai, T., Welf, E.S., David, A.F., Gerlich, D.W., Fiolka, R., Betzig, E., and Danuser, G. (2023). u-track3D: Measuring, navigating, and validating dense particle trajectories in three dimensions. Cell Rep. Methods *3*, 100655. https://doi.org/10.1016/j.crmeth.2023.100655.

34. Kubow, K.E., and Horwitz, A.R. (2011). Reducing background fluorescence reveals adhesions in 3D matrices. Nat. Cell Biol. *13*, 3–7. https://doi.org/10.1038/ncb0111-3.

35. Theodosiou, M., Widmaier, M., Böttcher, R.T., Rognoni, E., Veelders, M., Bharadwaj, M., Lambacher, A., Austen, K., Müller, D.J., Zent, R., and Fässler, R. (2016). Kindlin-2 cooperates with talin to activate integrins and induces cell spreading by directly binding paxillin. Elife *5*, e10130. https://doi.org/10.7554/eLife.10130.

36. Margadant, C., Kreft, M., de Groot, D.J., Norman, J.C., and Sonnenberg, A. (2012). Distinct roles of talin and kindlin in regulating integrin alpha5-beta1 function and trafficking. Curr. Biol. *22*, 1554–1563. https://doi.org/10.1016/j.cub.2012.06.060.

37. Harburger, D.S., Bouaouina, M., and Calderwood, D.A. (2009). Kindlin-1 and -2 directly bind the C-terminal region of beta integrin cytoplasmic tails and exert integrin-specific activation effects. J. Biol. Chem. *284*, 11485–11497. https://doi.org/10.1074/jbc.M809233200.

38. Grashoff, C., Hoffman, B.D., Brenner, M.D., Zhou, R., Parsons, M., Yang, M.T., McLean, M.A., Sligar, S.G., Chen, C.S., Ha, T., and Schwartz, M.A. (2010). Measuring mechanical tension across vinculin reveals regulation of focal adhesion dynamics. Nature *466*, 263–266. https://doi.org/10.1038/nature09198.

39. Carisey, A., Tsang, R., Greiner, A.M., Nijenhuis, N., Heath, N., Nazgiewicz, A., Kemkemer, R., Derby, B., Spatz, J., and Ballestrem, C. (2013). Vinculin regulates the recruitment and release of core focal adhesion proteins in a force-dependent manner. Curr. Biol. *23*, 271–281. https://doi.org/10.1016/j.cub.2013.01.009.

40. Hirata, H., Tatsumi, H., Lim, C.T., and Sokabe, M. (2014). Force-dependent vinculin binding to talin in live cells: a crucial step in anchoring the actin cytoskeleton to focal adhesions. Am. J. Physiol. Cell Physiol. *306*, C607–C620. https://doi.org/10.1152/ajpcell.00122.2013.

41. Thievessen, I., Fakhri, N., Steinwachs, J., Kraus, V., McIsaac, R.S., Gao, L., Chen, B.C., Baird, M.A., Davidson, M.W., Betzig, E., et al. (2015). Vinculin is required for cell polarization, migration, and extracellular matrix remodeling in 3D collagen. FASEB J. *29*, 4555–4567. https://doi.org/10.1096/fj.14-268235.

42. Gournier, H., Goley, E.D., Niederstrasser, H., Trinh, T., and Welch, M.D. (2001). Reconstitution of human Arp2/3 complex reveals critical roles of individual subunits in complex structure and activity. Mol. Cell *8*, 1041–1052. https://doi.org/10.1016/s1097-2765(01)00393-8.

43. Thompson, P.M., Tolbert, C.E., Shen, K., Kota, P., Palmer, S.M., Plevock, K.M., Orlova, A., Galkin, V.E., Burridge, K., Egelman, E.H., et al. (2014). Identification of an actin binding surface on vinculin that mediates mechanical cell and focal adhesion properties. Structure *22*, 697–706. https://doi.org/10.1016/j.str.2014.03.002.

44. Humphries, J.D., Wang, P., Streuli, C., Geiger, B., Humphries, M.J., and Ballestrem, C. (2007). Vinculin controls focal adhesion formation by direct interactions with talin and actin. J. Cell Biol. *179*, 1043–1057. https://doi.org/10.1083/jcb.200703036.

45. Jannie, K.M., Ellerbroek, S.M., Zhou, D.W., Chen, S., Crompton, D.J., García, A.J., and DeMali, K.A. (2015). Vinculin-dependent actin bundling regulates cell migration and traction forces. Biochem. J. *465*, 383–393. https://doi.org/10.1042/BJ20140872.

46. Janssen, M.E.W., Kim, E., Liu, H., Fujimoto, L.M., Bobkov, A., Volkmann, N., and Hanein, D. (2006). Three-dimensional structure of vinculin bound to actin filaments. Mol. Cell *21*, 271–281. https://doi.org/10.1016/j.molcel.2005.11.020.

47. Thievessen, I., Thompson, P.M., Berlemont, S., Plevock, K.M., Plotnikov, S.V., Zemljic-Harpf, A., Ross, R.S., Davidson, M.W., Danuser, G., Campbell, S.L., and Waterman, C.M. (2013). Vinculin-actin interaction couples actin retrograde flow to focal adhesions, but is dispensable for focal adhesion growth. J. Cell Biol. *202*, 163–177. https://doi.org/10.1083/jcb.201303129.

48. Alam, M.S. (2018). Proximity Ligation Assay (PLA). Curr. Protoc. Immunol. *123*, e58. https://doi.org/10.1002/cpim.58.

49. Ziegler, W.H., Liddington, R.C., and Critchley, D.R. (2006). The structure and regulation of vinculin. Trends Cell Biol. *16*, 453–460. https://doi.org/10.1016/j.tcb.2006.07.004.

50. Johnson, R.P., and Craig, S.W. (2000). Actin activates a cryptic dimerization potential of the vinculin tail domain. J. Biol. Chem. *275*, 95–105. https://doi.org/10.1074/jbc.275.1.95.

51. Kim, L.Y., Thompson, P.M., Lee, H.T., Pershad, M., Campbell, S.L., and Alushin, G.M. (2016). The Structural Basis of Actin Organization by Vinculin and Metavinculin. J. Mol. Biol. *428*, 10–25. https://doi.org/10.1016/j.jmb.2015.09.031.

52. Thompson, P.M., Tolbert, C.E., and Campbell, S.L. (2013). Vinculin and metavinculin: oligomerization and interactions with F-actin. FEBS Lett. *587*, 1220–1229. https://doi.org/10.1016/j.febslet.2013.02.042.

53. Shen, K., Tolbert, C.E., Guilluy, C., Swaminathan, V.S., Berginski, M.E., Burridge, K., Superfine, R., and Campbell, S.L. (2011). The vinculin C-terminal hairpin mediates F-actin bundle formation, focal adhesion, and cell mechanical properties. J. Biol. Chem. *286*, 45103–45115. https://doi.org/10.1074/jbc.M111.244293.

54. Tolbert, C.E., Burridge, K., and Campbell, S.L. (2013). Vinculin regulation of F-actin bundle formation: what does it mean for the cell? Cell Adh. Migr. *7*, 219–225. https://doi.org/10.4161/cam.23184.

55. Chorev, D.S., Volberg, T., Livne, A., Eisenstein, M., Martins, B., Kam, Z., Jockusch, B.M., Medalia, O., Sharon, M., and Geiger, B. (2018). Conformational states during vinculin unlocking differentially regulate focal adhesion properties. Sci. Rep. *8*, 2693. https://doi.org/10.1038/s41598-018-21006-8.

56. Lackner, D.H., Carré, A., Guzzardo, P.M., Banning, C., Mangena, R., Henley, T., Oberndorfer, S., Gapp, B.V., Nijman, S.M.B., Brummelkamp, T.R., and Bürckstümmer, T. (2015). A generic strategy for CRISPR-Cas9-mediated gene tagging. Nat. Commun. *6*, 10237. https://doi.org/10.1038/ncomms10237.

57. Welf, E.S., Driscoll, M.K., Dean, K.M., Schäfer, C., Chu, J., Davidson, M.W., Lin, M.Z., Danuser, G., and Fiolka, R. (2016). Quantitative Multiscale Cell Imaging in Controlled 3D Microenvironments. Dev. Cell *36*, 462–475. https://doi.org/10.1016/j.devcel.2016.01.022.

58. Mohan, A.S., Dean, K.M., Isogai, T., Kasitinon, S.Y., Murali, V.S., Roudot, P., Groisman, A., Reed, D.K., Welf, E.S., Han, S.J., et al. (2019). Enhanced Dendritic Actin Network Formation in Extended Lamellipodia Drives Proliferation in Growth-Challenged Rac1(P29S) Melanoma Cells. Dev. Cell *49*, 444–460.e9. https://doi.org/10.1016/j.devcel.2019.04.007.

59. Jaqaman, K., Loerke, D., Mettlen, M., Kuwata, H., Grinstein, S., Schmid, S.L., and Danuser, G. (2008). Robust single-particle tracking in live-cell time-lapse sequences. Nat. Methods *5*, 695–702. https://doi.org/10.1038/nmeth.1237.

60. Stringer, C., Wang, T., Michaelos, M., and Pachitariu, M. (2021). Cellpose: a generalist algorithm for cellular segmentation. Nat. Methods *18*, 100–106. https://doi.org/10.1038/s41592-020-01018-x.

61. Ran, F.A., Hsu, P.D., Wright, J., Agarwala, V., Scott, D.A., and Zhang, F. (2013). Genome engineering using the CRISPR-Cas9 system. Nat. Protoc. *8*, 2281–2308. https://doi.org/10.1038/nprot.2013.143.

62. Huisken, J., and Stainier, D.Y.R. (2007). Even fluorescence excitation by multidirectional selective plane illumination microscopy (mSPIM). Opt. Lett. *32*, 2608–2610. https://doi.org/10.1364/ol.32.002608.

63. Noh, J., Isogai, T., Chi, J., Bhatt, K., and Danuser, G. (2022). Granger-causal inference of the lamellipodial actin regulator hierarchy by live cell imaging without perturbation. Cell Syst. *13*, 471–487.e8. https://doi.org/10.1016/j.cels.2022.05.003.

64. Machacek, M., Hodgson, L., Welch, C., Elliott, H., Pertz, O., Nalbant, P., Abell, A., Johnson, G.L., Hahn, K.M., and Danuser, G. (2009). Coordination of Rho GTPase activities during cell protrusion. Nature *461*, 99–103. https://doi.org/10.1038/nature08242.

65. Dean, K.M., Roudot, P., Reis, C.R., Welf, E.S., Mettlen, M., and Fiolka, R. (2016). Diagonally Scanned Light-Sheet Microscopy for Fast Volumetric

Imaging of Adherent Cells. Biophys. J. *110*, 1456–1465. https://doi.org/10.1016/j.bpj.2016.01.029.

66. Gardel, M.L., Schneider, I.C., Aratyn-Schaus, Y., and Waterman, C.M. (2010). Mechanical Integration of Actin and Adhesion Dynamics in Cell Migration. Annu. Rev. Cell Dev. Biol. *26*, 315–333. https://doi.org/10.1146/annurev.cellbio.011209.122036.
67. Aguet, F., Antonescu, C.N., Mettlen, M., Schmid, S.L., and Danuser, G. (2013). Advances in Analysis of Low Signal-to-Noise Images Link Dynamin and AP2 to the Functions of an Endocytic Checkpoint. Dev. Cell *26*, 279–291. https://doi.org/10.1016/j.devcel.2013.06.019.
68. Lindeberg, T. (1998). Feature detection with automatic scale selection. Int. J. Comput. Vis. *30*, 79–116. https://doi.org/10.1023/a:1008045108935.
69. Frangi, A.F., Niessen, W.J., Vincken, K.L., and Viergever, M.A. (1998). Multiscale Vessel Enhancement Filtering (Springer Berlin Heidelberg), pp. 130–137.

STAR★METHODS

KEY RESOURCES TABLE

REAGENT or RESOURCE	SOURCE	IDENTIFIER
Antibodies		
mouse anti-mDia1/DIAPH1	BD Biosciences	Cat# BD 610848; RRID: AB_398167
mouse anti-ARP3 (A-1)	Santa Cruz	Cat# sc-48344; RRID: AB_626700
mouse anti-ARP3, (B-1)	Santa Cruz	Cat# sc-374200; RRID: AB_10990131
rabbit anti-Cofilin-1 D3F9	Cell Signaling Technology	Cat# 5175; RRID: AB_10622000
rabbit anti-alpha Actinin	Abcam	Cat# ab175944
mouse anti-FAK (D-1)	Santa Cruz	Cat# sc-271126; RRID: AB_10614323
mouse anti-FMNL1, (C-5)	Santa Cruz	Cat# sc-390023
mouse anti-FMNL2	Abcam	Cat# ab57963; RRID: AB_941625
rabbit anti-DIAPH3	ProteinTech	Cat# 14342-1-AP; RRID: AB_2092930
rabbit anti-INF2	Bethyl Laboratories	Cat# A303-428A; RRID: AB_10952400
mouse anti-FHOD1, (D-6)	Santa Cruz	Cat# sc-365437; RRID: AB_10843854
mouse anti-VASP	BD Biosciences	Cat# BD 610447
mouse anti-Mena (21)	Santa Cruz	Cat# sc-135988; RRID: AB_2098633
rabbit anti-Cortactin, [EP1922Y]	Abcam	Cat# ab81208; RRID: AB_1640383
mouse anti-CapZ-β, (52)	Santa Cruz	Cat# sc-136502; RRID: AB_10610091
rabbit anti-WAVE-2, (D2C8) XP	Cell Signaling Technology	Cat# 3659
rabbit anti-N-WASP (30D10)	Cell Signaling Technology	Cat# 4848
mouse anti-vinculin, (7F9)	Santa Cruz	Cat# sc-73614; RRID: AB_2941767
mouse anti-vinculin	Sigma-Aldrich	Cat# V9264; RRID: AB_10603627
mouse anti-Kindlin-2, clone 3A3	Millipore	Cat# MAB2617; RRID: AB_10631873
rabbit anti-p34-Arc/ARPC2	Millipore	Cat# 07-227
mNeonGreen-Trap Magnetic Agarose beads	Chromotek	Cat# ntma-20; RRID: AB_2827594
Chemicals, peptides, and recombinant proteins		
blasticidine S HCl	Thermo	R21001
Polyethylenimine	Sigma	408727
Platinum SuperFi II PCR Master Mix	Thermo	Cat # 12368010
AF488-conjugated Phalloidin	Thermo	A12379
AF568-conjugated Phalloidin	Thermo	A12380
Bovine collagen, Type 1	Advanced Biomatrix	Cat# 5133
rat-tail collagen	Corning	Cat# 354249
CK-666	Millipore	Cat# 182515
purified Arp2/3 complex	Cytoskeleton	RP-01-PA
QGel 920	CHT	QGel 920
20% Paraformaldehyde	Electron Microscopy Sciences	15713
Critical commercial assays		
Q5 site-directed PCR mutagenesis kit	NEB	E0554S
DNeasy Blood and Tissue kit	Qiagen	Cat # 69504
QIAquick Gel Extraction Kit	Qiagen	Cat # 28704
Duolink® *In Situ* Detection Red kit	Sigma	DUO92008
Experimental models: Cell lines		
U2OS	Gifted by Dick McIntosh (University of Colorado)	
RPE-1	ATCC	CRL-4000; RRID: CVCL_4388

(*Continued on next page*)

Continued

REAGENT or RESOURCE	SOURCE	IDENTIFIER
Oligonucleotides		
See Table S1 for oligonucleotides used	This paper	
Recombinant DNA		
pSpCas9(BB)-2A-GFP (PX458)	Addgene	#48138; RRID: Addgene_48138
psPax2	Addgene	#12260; RRID: Addgene_12260
pMD2.G	Addgene	#12259; RRID: Addgene_12259
pLVX-IRES-Puro	Takara Bio	Cat# 632183
pMA-tial1	Lackner et al.[56]	
F-tractin-GFP	Welf et al.[57]	
pLVX-CMV100-mNeonGreen-Paxillin-22	Mohan et al.[58]	
mNeonGreen-Vinculin-N-21	Allele Biotech	http://www.allelebiotech.com/mneongreen-fusions-and-constructs/
Software and algorithms		
MATLAB	The MathWorks, Inc	https://www.mathworks.com/
GraphPad Prism	GraphPad Software LLC	https://www.graphpad.com/
ImageJ		https://imagej.net/ij/
Illustrator	Adobe	https://www.adobe.com/
LabVIEW	National Instruments	https://www.ni.com/
ICE Analysis Software	Synthego	https://www.synthego.com/
2D and 3D PEI analysis	This paper	https://github.com/DanuserLab/Isogai-ARP23-Paper-2025
Focal Adhesion Segmentation	Han et al.[32]	https://github.com/DanuserLab
u-track Particle Tracking	Jaqaman et al.[59]	https://github.com/DanuserLab
u-track3D	Roudot et al.[33]	https://github.com/DanuserLab
cellpose	Stringer et al.[60]	https://github.com/MouseLand/cellpose

EXPERIMENTAL MODEL AND STUDY PARTICIPANT DETAILS

Cell lines and culture conditions

Human Osteosarcoma (U2OS; female) and human retinal pigment epithelial (RPE-1; female) cells were cultured in DMEM or RPMI media, respectively supplemented with 10% fetal bovine serum (Sigma; F0926-500ML) and maintained in a humidified incubator at 37°C and 5% CO_2. All cells were tested for mycoplasma using a Genlantis Mycoscope Detection Kit (MY01100). Cells were counted using Cellometer Auto 1000 Bright Field Cell Counter (Nexcelom). Stable cells expressing mNeonGreen-paxillin, and vinculin KO rescue cell lines were generated using lentiviral infection. mNeonGreen-paxillin expressing cells were FACS enriched. Stable vinculin KO rescue cell lines were enriched by puromycin selection (Figure S4D). U2OS cells were a kind gift from Dr. Dick McIntosh (University of Colorado, Boulder, CO). RPE-1 cells were purchased from ATCC. Cell lines were not authenticated.

METHOD DETAILS

Plasmids

Following plasmids were obtained from Addgene: pSpCas9(BB)-2A-GFP (PX458) (#48138), psPax2 (#12260), pMD2.G (#12259). Annealed gene-specific single guide RNAs (gRNAs) were cloned into the BbsI site of pSpCas9(BB)-2A-GFP (PX458).[61] mNeonGreen-Vinculin-N-21 (full-length human cDNA with inherent V234L mutation) C-terminally tagged with mNeonGreen spaced with a 21-amino acid linker was from Allele Biotech. mNeonGreen-vinculin was subcloned into the lentiviral pLVX-IRES-Puro vector (Takara Bio) and sequence verified with Sanger sequencing. Subsequent vinculin mutants were generated using the Q5 site-directed PCR mutagenesis kit (NEB) and sequence verified. The self-cleaving vector pMA-tial1 was from Tilmann Bürckstümmer. F-tractin-GFP was previously described.[57] pLVX-CMV100-mNeonGreen-Paxillin-22 was previously described.[58] All primers used in this study are listed in Table S1.

Generation of knockout cell lines

1 x 10^5 U2OS cells were seeded in a 6 well plate and transiently transfected overnight with plasmid PX458 containing a gene-specific sgRNA (Table S1), together with a modified self-cleaving donor vector[56] containing a blasticidin-resistance gene (*bsr*) cassette using

Polyethylenimine (Sigma; 408727). Cells transfected with SpCas9 only (no sgRNA) in combination with the *bsr* donor vector served as a negative control. The following day, the cell media was replaced. For selection, equal number of cells were seeded in a 15 cm dish in media containing 5 μg/mL blasticidine S HCl (Thermo; R21001) until the negative control was completely absent of cells. Single clonal colonies were isolated using Pyrex Cloning Cylinder (Sigma, CLS31666), and gene knockouts verified with Western Blotting. Antibodies used to verify the knockouts are listed in key resources table and Table S2.

CRISPR knockout validation

PCR primers were designed 200–300 bp upstream and downstream of Cas9 cut sites and verified for specificity using primer-BLAST. Genomic DNA of wild-type and CRISPR edited cells was isolated using DNeasy Blood and Tissue kit (Qiagen, Cat # 69504) and quantified using nano-drop. PCR was performed using Platinum SuperFi II PCR Master Mix (Thermo, Cat # 12368010) and verified on 1% agarose gel. Amplified fragments were gel purified (QIAquick Gel Extraction Kit, Cat # 28704) and sent for sanger sequencing. The sequences were analyzed and verified using Synthego's ICE Analysis software (https://www.synthego.com/) for knockout screening and confirmed for frameshifts using serial cloner. Primers used for CRISPR knockout verification by PCR amplification are listed in Table S1. Validation of key cell lines are reported in Figure S6.

Two-dimensional PEI assay

Bovine collagen-coated (2 μg/mL) coverslips were placed in a 6 well plate, seeded with 1.0 x 10^5 cells, and allowed to spread overnight. Cells were fixed with pre-warmed 4% paraformaldehyde at 37° for 10 min. Fixed cells were permeabilized with 0.1% Triton X-100 for 10 min and stained with AF488-conjugated Phalloidin (Thermo; A12379, 1:40 dilution) for 1 h. Images were acquired with an inverted Nikon Ti-E microscope at 10X magnification (Nikon 10X NA 0.25) and collected on a scientific complementary metal oxide sensor with 6.5-micron pixels, and a field of view of 2560x2160 pixels (Zyla, Andor).

Large field-of-view LSFM (IFOV-LSFM)

For high-throughput morphological screening of knock-out cell lines, a dual-illumination light-sheet fluorescence microscope (LFSM) was built that permits scanning of the beam in the Z-dimension as well as pivoting the light-sheet in the sample-plane to reduce shadowing and stripe artifacts.[62] For illumination, 405 nm, 488 nm, 561 nm, and 640 nm lasers (OBIS LS and LX, Coherent, Inc.) are combined with dichroic mirrors (MUX Series, Semrock), spatially filtered and expanded with a telescope consisting of a 50 mm achromatic convex lens (AC254-050-A-ML, ThorLabs, Inc.), a 100-micron pinhole (P100H, ThorLabs, Inc.), and a 400 mm achromatic convex lens (AC254-400-A, ThorLabs, Inc.). An achromatic Galilean beam expander (GBE02-A, ThorLabs, Inc.) further increases the laser diameter 2x. All solid-state lasers are directly modulated with analog signals originating from a field-programmable gate array (PCIe-7252R, National Instruments) that have been conditioned with a scaling amplifier (SIM983 and SIM900, Stanford Research Systems).

For light-sheet generation, a 50 mm focal length cylindrical lens (ACY254-050-A, ThorLabs, Inc.) is used to focus the laser illumination into a sheet that is relayed to the 10X NA 0.28 illumination objective (M Plan Apo 10x, 378-803-3, Mitutoyo) with two mirror galvanometers (GVS001, ThorLabs, Inc.), a 50 mm achromatic convex lens (AC254-050-A, ThorLabs, Inc.), a 100 mm achromatic convex lens (AC508-100-A, ThorLabs, Inc.), and a 200 mm focal length tube lens (ITL-200, ThorLabs, Inc.). The Z-galvanometer is conjugated to the back pupil of the illumination objective, whereas the pivot galvanometer is conjugated to the sample plane. To control the light-sheet thickness, a variable slit (VA100C, ThorLabs, Inc.) was placed in the back-pupil plane of the cylindrical lens, which is conjugated to the back-pupil planes of the illumination objective.

For detection, a 16X NA 0.8 objective lens (CFI75 LWD 16XW, Nikon Instruments) and a 200 mm focal length tube lens (58–520, Edmund Optics Inc.) form the image on a sCMOS camera (ORCA-Flash4.0, Hamamatsu Photonics). A laser line filter (ZET405/488/561/640, Chroma Technology Corporation) is placed after the detection objective lens and a filter wheel (Lambda 10-B, Sutter Instrument Company) equipped with multiple bandpass filters is placed between the tube lens and the camera. The detection objective lens is mounted on a piezo-driven stage (Nano-F450, Mad-City Labs Inc.) that provides 450 μm travel range. The sample stage is a combination of a three-axis motorized stage (MP285, Sutter Instrument Company) and a rotation stage (U-651.03, Physik Instrumente). The microscope is controlled by custom software (LabView, National Instruments).

Sample preparation for 3D imaging

3D samples were prepared by embedding cells at a final concentration of approximately 6.7 x 10^5 cells/ml in 3 mg/mL rat-tail collagen (Corning; 354249). 3D samples were polymerized into a custom-made 3D sample holder, by placing the holder in a 6 wells plate and at 37°C for up to 10 min. Once the collagen polymerized, 4 mL of media was added to the well to avoid drying of the gel and incubated overnight in the incubator to allow cell spreading. The following day, cells were fixed with pre-warmed 4% paraformaldehyde for 30 min at 37°C. Fixed gels were permeabilized with 0.1% Triton X-100 for 30 min, and subsequently stained with AF488- or AF568-conjugated Phalloidin (Thermo; A12379, A12380).

Pharmacological perturbations

The Arp2/3 Complex inhibitor CK-666 was from Millipore (182515) and was used at 100 μM and 250 μM. For treatment of cells in 3D, inhibitor-containing media was added to the cells as soon as the collagen gel was polymerized.

Analysis of protrusion dynamics in 2D

U2OS wild-type and Arp3 KO #1 cells expressing F-tractin-GFP were seeded and imaged on glass coverslips coated with 2 μg/mL collagen-I and imaged on a Nikon EclipseTi-E inverted microscope coupled to an Andor Diskovery TIRF/Borealis widefield illuminator equipped with an additional 1.8x tube lens (yielding a final magnification of 108x). The microscope was equipped with a 60x Nikon 1.49 NA TIRF DIC objective, Andor Zyla 4.2 16 bit, 100 fps, 2048x2048 px sCMOS cameras, and environmental chamber was custom built by OKO lab with temperature control and CO_2 stage incubator.

To study membrane protrusion dynamics, we computationally tracked the cell boundary movements over time using a previously described software.[63] The cell boundaries were segmented by thresholding tractin-GFP intensity and we computed the autocorrelation function (ACF) of the edge velocity in each cell to determine the time lag with the largest negative autocorrelation, which corresponded to the half-life ($t_{1/2}$) of a protrusion/retraction cycle.[64]

2D TIRF imaging of focal adhesions

Cells were imaged with a DeltaVision OMX SR (General Electric) equipped with ring-TIRF, which mitigates laser coherence effects and provides a more homogeneous illumination field. This microscope is equipped with a 60x, NA = 1.49, objective, and 3 sCMOS cameras, configured at a 95 MHz readout speed to further decrease readout noise. Images 1024x1024 pixels were acquired with an effective pixel size of 80 nm. Imaging was performed at 37°C, 5% carbon dioxide, and 70% humidity. Laser-based identification of the bottom of the substrate was performed prior to image acquisition, with a maximum number of iterations set to 10. Laser powers were decreased as much as possible (usually between 0.2 and 2%).

High-resolution focal adhesion imaging in 3D

For high-resolution adhesion imaging in 3D, a high-NA version of Axially Swept Light-Sheet Microscopy was developed.[9,65] Illumination is provided with 445 nm, 488 nm, 514 nm, 561 nm, and 640 nm lasers (OBIS LS and LX, Coherent, Inc.), which are co-aligned with dichroic mirrors (MUX Series, Semrock), spatially filtered and expanded with a telescope consisting of a 50 mm focal length achromatic convex lens (AC254-050-A-ML, ThorLabs), a 30 μm pinhole (P30H, ThorLabs, Inc.), and a 150 mm focal length achromatic convex lens (AC254-150-A, ThorLabs). Laser polarization was controlled with a half waveplate. All solid-state lasers are directly modulated with analog signals originating from a field-programmable gate array (PCIe-7252R, National Instruments) that have been conditioned with a scaling amplifier (SIM983 and SIM900, Stanford Research Systems).

For light-sheet generation, a 50 mm focal length cylindrical lens (ACY254-050-A, ThorLabs, Inc.) is used to focus the laser illumination into a sheet. A mechanical slit (VA100C, ThorLabs, Inc.) conjugate to the back pupil of the cylindrical lens was used to adjust the effective numerical aperture of the light-sheet, and a diffraction grating at the focus on the cylindrical lens was used to create a lattice of coherent Gaussian beams. The light-sheet was relayed to the first intermediate image plane with a 75 mm achromatic doublet (AC254-050-A, ThorLabs, Inc.), a matched pair of 3 mm mirror galvanometers (6215H, Cambridge Technology) conjugate to the back pupil of the cylindrical lens, and a 60 mm focal length f-theta scan lens (S4LFT0061/065, Sill Optics). One galvo laterally scans the lattice of Gaussian beams in the X-direction and create a time-averaged light-sheet with decreased susceptibility to shadowing artifacts, and the other galvo scans the light-sheet in the Z-direction. The first intermediate image plane was relayed to a small aperture remote-focusing mirror (PF03-03-F01, ThorLabs, Inc.) with a 100 mm achromatic doublet lens (AC254-100-A, ThorLabs, Inc.) and a 40X 0.6 NA air-immersion objective (CFI S Plan Fluor ELWD, Nikon Instruments). Prior to being focused by the objective, the light passes through a polarizing beam splitter and an achromatic quarter-wave plate, which are located in the infinity space of the objective. The mirror, located at the focus of the air-immersion objective, reflects light back through the objective, which is subsequently passed through the same achromatic quarter-wave plate, reflected by the polarizing beam splitter, and focused to the second intermediate image plane with another 100 mm achromatic doublet. Displacement of the mirror with a piezo actuator (P-603.1S2 and E−709.SRG, Physik Instrumente) results in a wavefront that deterministically scans the light-sheet along its propagation axis (e.g., the Y-dimension). Lastly, the second intermediate image plane was imaged to the sample plane with a 200 mm tube lens (ITL200, ThorLabs, Inc.) and an NA 0.71 water dipping illumination objective (54-10-7, Special Optics).

For detection, a 25X NA1.1 water-dipping objective lens (CFI75 Apo LWD 25XW, Nikon Instruments) and a 500 mm achromatic doublet (49–396, Edmund Optics) creates an image which is spectrally separated with a dichroic mirror on two sCMOS cameras (ORCA-Flash4.0, Hamamatsu Photonics). A laser line filter (ZET405/488/561/640, Chroma Technology Corporation) is placed after the detection objective lens. The detection objective lens is mounted on a piezo-driven stage (P-726 PIFOC High-Load Scanner, Physik Instrumente) that provides 100 μm travel range. The sample stage is a three-axis motorized stage (Sutter Instrument, MP285), and the microscope is controlled by the custom LabVIEW software (Coleman Technologies, National Instruments).

Pull-down assay

U2OS vinculin KO cells rescued with respective mNeonGreen-tagged full-length vinculin constructs were seeded overnight (~8.0 x 10^6) and lysed with 300 μL ice-cold Lysis buffer (10 mM Tris-HCl, pH 7.5, 150 mM NaCl, 0.5 mM EDTA, 0.5% Nonidet P-40) supplemented with protease inhibitors and 1 mM PSFM. The lysates were pre-cleared with protein A Sepharose beads for 1h at 4°C. 2% of the pre-cleared lysates were saved for further input fraction analysis. Following the pre-clearing step, mNeonGreen-tagged vinculin was immunoprecipitated by incubating 1 μg of the pre-cleared lysates with mNeonGreen-Trap Magnetic Agarose beads (Chromotek, ntma-20) for 2h at 4°C. The mNeonGreen vinculin-bound beads were washed three times with the Lysis Buffer and incubated with

2 μg of purified Arp2/3 complex (RP-01-PA Cytoskeleton) for 24 h at 4°C. The beads were gently washed twice with 500 μL ice-cold Wash buffer (10 mM Tris-HCl pH 7.5, 150 mM NaCl, 0.5 mM EDTA) and separated by SDS-PAGE for Western Blot analysis.

p34-ARC-vinculin proximity ligation assay (PLA)

U2OS vinculin KO cells rescued with designated mNeonGreen-tagged vinculin mutants or empty vector control cells were mixed at a ratio 1:1 and seeded on 2 μg/mL collagen-coated glass or QGel 920-covered glass-bottom dishes (Greiner Bio-One). QGel 920 was mixed at a solution A to B ratio of 1:1.15 yielding an approximately 8 kPa gel as previously described.[31,32] Cells were allowed to spread overnight and fixed in pre-warmed 4% paraformaldehyde (PFA)/PBS (v/v) for 10 min at 37°C. Fixed samples were permeabilized with 0.1% Triton X-100/PBS (v/v) for 10 min at room temperature (RT). The Duolink *In Situ* Detection Red kit (Sigma-Aldrich; DUO92008) was used according to the manufacturer's guidelines: samples were blocked in Duolink Blocking Solution for 30 min at RT. Subsequently, the samples were stained with rabbit anti-p34-ARC/ARPC2 (Millipore; 07–227; 1:250) and mouse anti-vinculin (Sigma-Aldrich; V9264; 1:500) for 1 h at RT, followed by 1 h RT incubation with the Duolink PLA probes, 30 min ligation and 200 min amplification at 37°C in a humidified chamber. Epifluorescence images were collected on the TIRF microscope mentioned earlier.

QUANTIFICATION AND STATISTICAL ANALYSIS

Two-dimensional PEI analysis

To evaluate pseudopod extensions in two-dimensional environments, images from the two-dimensional PEI assay were automatically evaluated with a script written in MATLAB (Mathworks, Inc) available under https://github.com/DanuserLab/Isogai-ARP23-Paper-2025. Specifically, data were loaded, and foreground-background segmented using morphological opening and closing based on morphological reconstruction using a disk shaped structuring element. Foreground objects, i.e., cells, were marked, holes filled, and clusters of cells were removed based on size. All cells touching the edge of the field of view were excluded from analysis. The convex area and area were measured for each segmented object and were used to compute the Pseudopod Extension Index (PEI; Convex Area divided by Segmented Area). The PEI of a particular perturbation condition was normalized with the experimental control, in most cases the wild-type control cells unless otherwise indicated. Each image (field of view) instead of each individual cell was considered as a technical replicate and data point. Thus, each data point represents the median PEI of dozens of cells, which also serves to reduce noise due to imperfect segmentation.

Three-dimensional PEI analysis

To evaluate pseudopod extensions in three-dimensional environments, we imaged 3D-collagen embedded cells with the lFOV-LSFM and measured PEI using a custom image analysis script developed in MATLAB (Mathworks, Inc.) available under https://github.com/DanuserLab/Isogai-ARP23-Paper-2025. Briefly, the 0.05% brightest pixels (i.e., the mean plus four standard deviations) were used as an initial mask for the cells. Small features in the segmented objects were removed, holes in the segmented features were filled, and segmented objects touching the edge of the field of view were excluded from analysis. The Convex Volume and Segmented Volume were measured for each segmented object, and the PEI was calculated by taking the ratio between Convex Volume and Segmented Volume. Normalized PEI was calculated by normalizing all values with the experimental control, in most cases the wild-type control cells unless otherwise indicated. Each 3D image stack, i.e., one image field of view rather than each individual cell was considered as a technical replicate and data point. Thus, each data point represents the median PEI of dozens of cells, which aids to reduce quantification errors due to imperfect segmentation in 3D.

Focal adhesions analysis in 2D

Cell-matrix nascent adhesions (NAs) from TIRF images were detected and segmented as diffraction-limited objects, and mature focal adhesions (FA) were detected as previously described.[32] Briefly, adhesions from images with paxillin staining were segmented using a combination of Otsu and Rosin thresholds. Segmented areas larger than 0.2 μm^2 were considered focal contacts (FCs) or FAs, based on the criteria described by Gardel et al.[66] Individual segmentations were assessed for the area and the length, which is estimated by the length of major axis in an ellipse that fit in each FA segmentation. FA density was calculated as the number of all segmentations divided by the cell area. Nascent adhesions were detected using the point source detection used in single particle tracking.[67] Briefly, mNeonGreen-paxillin images were filtered using a Laplacian of Gaussian filter, local maxima were detected and fitted with an isotropic Gaussian function (standard deviation: 2.1 pixel). Outliers were removed using a goodness of fit test ($p = 0.05$). NA density was defined as the number of NAs divided by the cell area derived from 5 μm from the segmented cell border. All densities were normalized to the corresponding wild-type control.

Focal adhesion characterization in 3D

Cell-matrix adhesions were detected in a fully-automated format using the multiscale detector implemented in the u-track3D software package.[33] This detector can identify adhesions of multiple sizes down to dim, diffraction-limited structures. Briefly, to adapt to multiple object sizes, the detector operates in a multiscale Laplacian of a Gaussian filtering framework[68] to estimate a scale-space signature map for each voxel and scales ranging from 100 nm to 5 microns. Excluding boundaries, local maxima in the scale-space

map represents candidate adhesion locations and scale. Each scale filtering response needs to be normalized to determine the most likely scale at each location. We found that normalizing by the L1 norm of the convolution filter provided best results. In order to label voxels pertaining to the background or an adhesion structure, we exploited an adaptive thresholding approach process described in.[67] Adhesion clusters were separated by the watershed segmentation. For each detected adhesion, the elongation was estimated by averaging a tubularity metric measured on each voxel associated to a single adhesion. The tubularity metric is inspired by the classic vesselness estimator by,[69] and adapted to discriminate between flat and elongated adhesions. Let ($\lambda_1<\lambda_2<\lambda_3$) be the three eigenvalues of the Hessian matrix computed at each voxel of an adhesion, we compute tubularity metric T in the range [0 … 1]:

$$T = 1 - \left|\frac{\lambda_1}{\lambda_2}\right|$$

For each acquisition of a complete 3D cellular volume, the distribution of adhesion elongation per cell is estimated using a kernel smoothing function equipped with a bandwidth that is optimal under a normal distribution assumption.

We assessed the significance of the differences between adhesion elongation distribution in control and treated conditions by performing 100 two-sampled t-tests for 100 elongation values ranging between 0 and 1. The resulting set of *p*-values describes the range of elongation values where the difference between conditions is significant.

To further confirm that the alleged differences between the elongation distributions of wild-type (WT) and Arp3 KO cells are significant we used the Kolmogorov-Smirnov (K-S) single-tailed test. It is well known, however, that the K-S test is very sensitive and may also detect a significant difference between two WT cells. Thus, we recalibrated the K-S test for our data by comparing the distribution of K-S statistic measured in-between individual WT cell adhesion elongation distributions to the K-S statistics measured between pairs of control and Arp3 KO cells. We show that the "WT vs. WT" group of K-S statistics is significantly lower (t-test: $p < 10^{-9}$) than the "WT vs. Arp3 KO" group.

p34-ARC-vinculin PLA analysis

Individual cells were segmented using cellpose.[60] Cells with bad segmentations were discarded. In some cases, a cell was wrongly segmented into smaller pieces due to a watershed failure, and in those cases the masks were merged (Figure S5A). The mNeonGreen localization pattern (homogenously diffuse versus localization to FAs and/or excluded from the nucleus) allowed us to distinguish empty vector control from vinculin mutant-rescued cells, respectively, and were manually annotated. Uncertain cases were omitted from the analyses. p34-ARC-vinculin PLA puncta were detected using the single particle detection algorithm implemented in the u-track package.[59] The total number of puncta was computed per cell and normalized to their respective cell area. Given the inherent heterogeneity of the PLA reaction per coverslip, the mean PLA density from the respective empty vector control was subtracted from the PLA density of the vinculin rescue samples to account for per-coverslip reaction variation. Therefore, in some cases, the PLA density could be negative. Finally, all data was normalized to the respective experimental mean of the wild-type vinculin rescued cells. Each datapoint represents a cell.

Statistical analysis

Data are presented as scatterplots (except for Figure 3B represented with bar graphs), with mean ± standard deviation (s.d.) or standard error of mean (s.e.m.), as indicated in the legends. The number of biological repeats (N) are denoted in the legends. Technical replicas (n), which either are represented by a field-of-view or an individual cell specified in the figure legends, are shown on the graph plots. *p* values were computed using the GraphPad Prism software (version 10, GraphPad Software Inc.) and reported alongside the statistical tests used in the figure legends.